Synthesis and Electronic Transport of Natural Superlattice Compounds

by

Alan Chen

B.S., Engineering Physics, Cornell University (2020)

Submitted to the Department of Electrical Engineering and Computer Science
in partial fulfillment of the requirements for the degree of

Master of Science

at the

MASSACHUSETTS INSTITUTE OF TECHNOLOGY

September 2023

Authored by:	Alan Chen Department of Electrical Engineering and Computer Science August 31, 2023
Certified by:	Joseph Checkelsky Associate Professor of Physics Thesis Supervisor
Accepted by:	Leslie A. Kolodziejski Professor of Electrical Engineering and Computer Science Chair, Department Committee on Graduate Students

Synthesis and Electronic Transport of Natural Superlattice Compounds

by

Alan Chen

Submitted to the Department of Electrical Engineering and Computer Science on August 31, 2023 in partial fulfillment of the requirements for the degree of

Master of Science

ABSTRACT

The study of periodic structures and their impact on states of matter is essential in condensed matter physics. The analysis of this periodicity led to the modern understanding of electronic properties through the band structure. Advances in materials synthesis and discovery have led to precise control over electronic properties via control of the atomic structure. One family of materials in which this has been explored are van der Waals (vdW) materials. In addition to their study as bulk crystalline specimens, the two-dimensional nature of these materials enables the development of artificial heterostructures with a diverse range of electronic states of matter. The ability to in turn design bulk crystals containing such heterostructures would enable access to a broader range of experimental techniques and potential new electronic states. In this thesis, we present a synthesis study of natural superlattices composed of transition metal dichalcogenide (TMD) monolayers alternating with spacer layers. These superlattices belong to the TMD family with chemical formula $M\mathrm{S}_2$, M = (V, Nb, Mo, W). We study one such compound, Sr-VS_2, through electronic transport measurements including evidence for an insulating state therein. We further discuss syntheses of Group-VI TMD superlattices and the potential physics such systems may support.

Thesis supervisor: Joseph Checkelsky
Title: Associate Professor of Physics

Acknowledgments

I would like to thank my advisor, Professor Joseph Checkelsky, for his support and mentorship in the past two years at MIT. Joe has taught me how to become a better experimental physicist. Joe is patient and empathetic advisor on top of his acuity as a scientist. His willingness to scrutinize experimental data has honed my experimental skills in the lab, while his ability to discuss overarching ideas and goals has kept me from getting lost in the weeds.

I also wish to thank the members of the Checkelsky group with whom I have spent a great deal of time. I would like to thank Joshua Wakefield for his mentorship in crystal growth and transport. Josh has been patient and insightful throughout the different projects I have undertaken while in the group, and he has always offered generous amounts of his time to guide me on my experiments. I thank Takehito Suzuki for his expanse knowledge in crystal growth and for entertaining my own naive ideas. I would like to also thank Frank Shu Yang Zhao for the many discussions on natural superlattices. His willingness to tackle the challenging questions associated with them has been a source of motivation. I thank Paul Neves, Caolan John, Aravind Devarakonda, Kent Jingxu Zheng, and Max Debbas for teaching me many of the experimental techniques I regularly employ now. I thank Mingyong Han, Boris Tsang, Pheona Williams, Shiang Fang, Ryan McTigue, and other members of the Checkelsky group for both insightful and fun discussions.

I am grateful for the opportunity to participate in multiple experiments at the National High Magnetic Field Lab (Maglab), where I have learned many of the intricacies in sample preparation, careful transport measurements, and data analysis. I thank Dave Graf for his knowledge and support during our trips to Tallahassee. I thank Gerry Miller for her administrative support and Professor Tomas Palacios for his academic advice.

I would like to thank Matthew, Kevin, Eliana, Ilia, Mufan, Caroline, and many others for their friendship these past two years. I am grateful to Anvita for keeping me grounded through both calm and difficult times. Finally, I wish to thank my family for their steadfast support and companionship.

Contents

List of Figures

List of Tables

Chapter 1

Introduction

1.1 Periodic modulations in condensed matter systems

Periodicity plays a fundamental role in the electronic properties of crystalline materials. The development of Bloch's theorem led to the modern understanding of electronic band structures. In addition to the periodicity of the atomic lattice, periodicity of quasiparticles in condensed matter systems create additional modifications to the electronic structure. Periodic structures may also arise as superstructures of the crystal, such as in the form of a charge density wave (CDW) [1].

A crystal may develop a CDW through electron-phonon coupling. This was observed in several compounds with one-dimensional (1D) chains, such as the organic salt tetrathiafulvalenetetracyanoquinodimethane (TTF-TCNQ), connecting to the Peierls distortion in an infinite 1D atomic chain [6][7]. In 2D and 3D, it is also possible to realize a CDW if there is an instability either through Fermi surface nesting or electronic correlations.

Another pathway towards the formation of periodic modulations arose from the development of molecular beam epitaxy (MBE). The ability to deposit materials in a layered, epitaxial manner enabled the growth of artificial lattices, and in turn new electronic states of matter. This technology led to the growth of highly clean GaAs/AlGaAs interfaces, which realized a 2D electron gas. The high degree of control of these heterostructures led to the discovery of the fractional quantum Hall effect (FQHE)[8]. The quality of the interface is crucial to creating high mobility samples. Further improvements to the controlled synthesis have led to recent reports of anyon braiding for topological quantum computation or exotic many-body phases such as Wigner crystals, stripes, bubbles, and nematic order [9].

The discovery of a 2D gas exhibiting the quantum Hall effect in graphene opened a new family of materials for studying low-dimensional electronic states [10][11]. In contrast to the 2DEGs formed through epitaxial growth, graphene can readily be prepared through mechan-

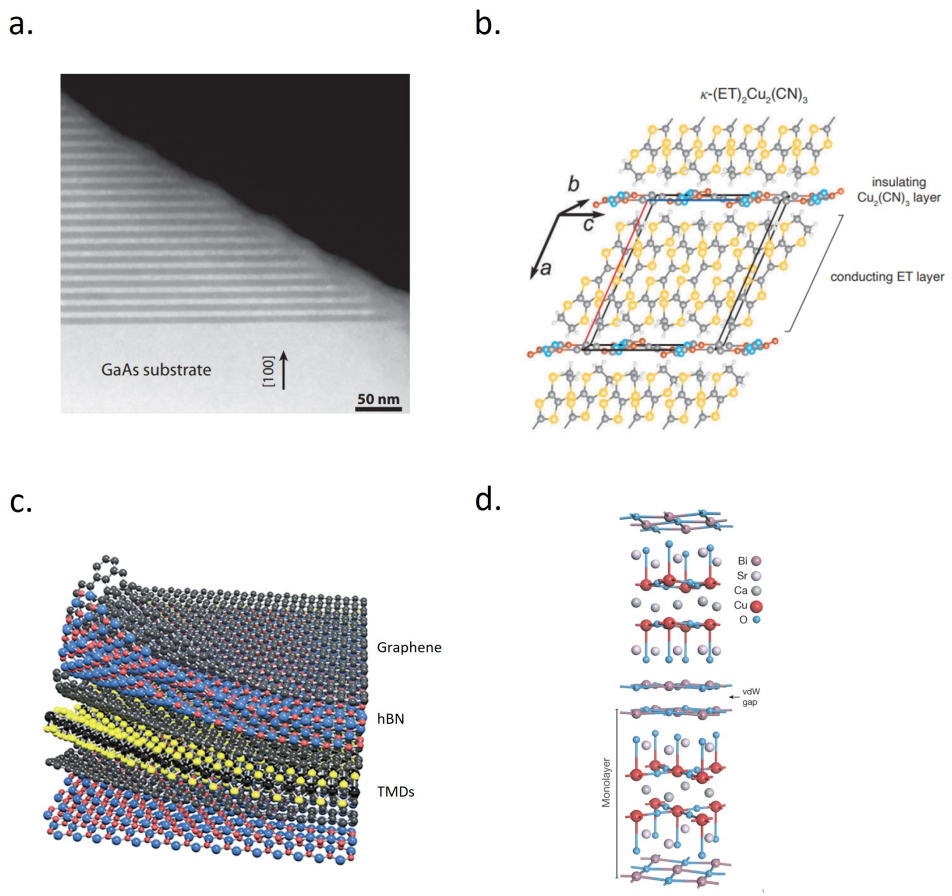

Figure 1.1: **a** GaAs/AlGaAs heterostructure grown through MBE. Adapted from [2]. **b** Organic superconductor containing alternating insulating and superconducting layers. Adapted from [3]. **c** van der Waals heterostructures in 2D assembled through stacking of monolayers. Adapted from [4]. **d** Layered high-temperature superconductor $Bi_2Sr_2CaCu_2O_{8+\delta}$. Adapted from [5].

ical exfoliation. Unique to these van der Waals crystals is the fact that they can be stacked together to form artificial heterostructures without need for epitaxy. Furthermore, these heterostructures often have atomically sharp interfaces as the crystals consist of single layers of atoms. The combination of these factors led to a broad range of new superlattices, which have driven a plethora of discoveries, such as of FQHE in graphene, black phosphorous, and black arsenic [12][13][14]. In addition, vdW crystals have served as valuable probes of 2D magnetism, optoelectronics, topology, and superconductivity[15][16][17].

Taking the vdW systems a step further, layers of graphene may be stacked with a twist angle, creating a small lattice mismatch that results in a long wavelength modulation, known as a moiré pattern. The size of the moiré cell in these heterostructures is controlled by the

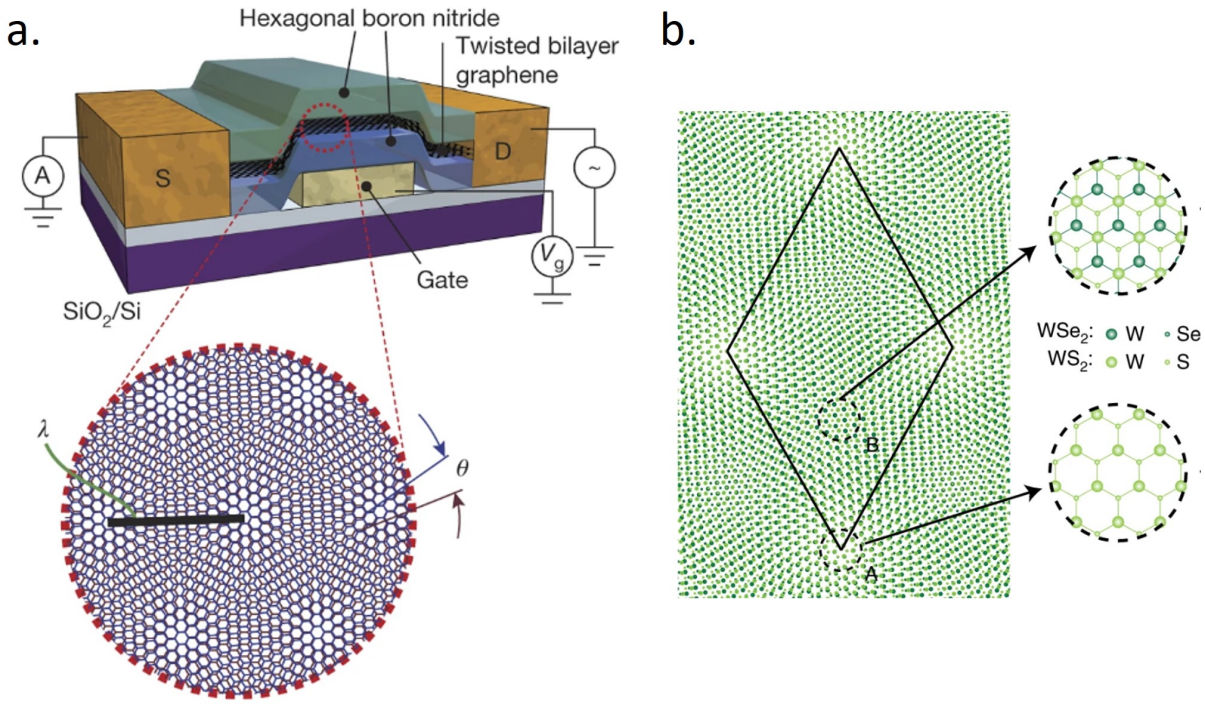

Figure 1.2: **a** Moiré pattern in twisted bilayers of graphene. **b** Moiré pattern in TMD (WSe_2 and WS_2) bilayers with lattice mismatch. Adapted from [18] (**a**) and [19] (**b**).

lattice constants of the stacked layers and the relative angle at which they are aligned. Such superlattices host correlated insulator and superconducting phases [20]. These many-body states are created due to the strong interactions arising from a flat band created near the Fermi level. The narrow bandwidth contains a large density of states, which in turn promotes interaction between the electrons. The additional degree of freedom in twist angle enabled study of more exotic phases of matter. The combined control of twist angle, atomic composition, and Fermi level through electrostatic doping have led to observations of orbital ferromagnetism, fractional Chern insulators, and stripe order[21]. Recently, twisted homobilayers of TMDs have been reported to exhibit fractional quantum anomalous Hall effect (FQAHE), underscoring the wealth of physics that can be accessed through these 2D systems[22].

Similarities have been noted between vdW heterostructures and the families of high temperature superconductors (HTS). For one, many of these HTS's, such as the cuprates, consist of layers of CuO_2 planes which form a 2D square lattice[23]. These planes are responsible for the unconventional superconductivity and have 2D electronic properties. At the same time, there are distinctions. Whereas vdW structures require careful exfoliation and assembly to realize the delicate electronic states, natural bulk superlattices can be synthesized

through chemical means via traditional crystal growth processes. Furthermore, their properties are accessible to characterization techniques which require bulk crystals. For example, X-ray and neutron scattering provide insight into structural properties of the material, while torque magnetometry and SQUID measurements provide characterization of magnetism in these structures. Thermodynamic probes such as heat capacity are also reliant on bulk single crystals and can reveal valuable information on phase transitions in the material.

One natural superlattice compound synthesized is $Ba_6Nb_{11}S_{28}$ [24]. The crystal contains monolayers of TMD NbS_2 stacked alternately with an insulating spacer. Like its parent TMD, $Ba_6Nb_{11}S_{28}$ is a superconductor with a quasi 2D Fermi surface. The spacer layer is commensurate with the TMD layer, creating a zone folding that leads to enhanced superconductivity in the *ab*-plane of the crystal. Furthermore, in magnetic field $Ba_6Nb_{11}S_{28}$ hosts signatures of a spatially modulated superconducting state known as the Fulde-Ferrell-Larkin-Ovchinnikov (FFLO) state [25]. $Ba_6Nb_{11}S_{28}$ also hosts Rashba spin-orbit coupling (SOC) in the band structure. These phenomena are influenced by the spacer, whose commensurate nature leads to zone folding of the NbS_2 bands. The observation of this finite-momentum superconductivity hints at the existence of other superconducting phases in natural superlattices.

In this thesis, we explore the synthesis of TMD superlattice compounds and their electronic properties. We observe signs of a correlated insulator phase, probed by electronic transport. In addition, we explore the effect of magnetism in this superlattice motif. We expand upon a family of natural superlattices, which are host to exotic phases of matter not found in the parent TMD. This provides an avenue to robustly engineer such phases and study them with bulk experimental probes to reveal potential new physics.

1.2 Unconventional Superconductors and Correlated Insulators

Superconductivity was first discovered in Hg in 1911. At the critical temperature T_C, the resistance drops to zero. It was over forty years before the first microscopic theory for superconductivity was developed by Bardeen, Cooper, and Schrieffer (BCS)[26]. The BCS theory describes the superconducting phase as a quantum phase consisting of quasiparticles formed from pairs of electrons. These Cooper pairs are bound by an attractive potential,

$$V_{int} = \frac{1}{2V} \sum_{k_1,k_2,q} \sum_{\sigma_1,\sigma_2} V_c(\mathbf{q}) c^\dagger_{k_1-q,\sigma_1} c^\dagger_{k_2+q,\sigma_2} c_{k_2,\sigma_2} c_{k_1,\sigma_1}, \tag{1.1}$$

where $V_C(\mathbf{q})$ represents the interaction potential between electrons, and $c^\dagger_{k,\sigma}, c_{k,\sigma}$ represent the creation and annihilation operators for an electron of momentum k and spin σ, respectively. The BCS Hamiltonian is

$$H = \sum_{k\sigma} \xi_k c^\dagger_{k\sigma} c_{k\sigma} + \frac{1}{N} \sum_{kk'} V_{kk'} c^\dagger_{k\uparrow} c^\dagger_{-k\downarrow} c_{k\downarrow} c_{k\uparrow}. \tag{1.2}$$

This equation can be solved with a mean field approximation to obtain a gap equation

$$\Delta_k = -\frac{1}{N} \sum_{k'} V_{kk'} \frac{\Delta_{k'}}{2E_{k'}} [1 - n_F(E_{k'})]. \tag{1.3}$$

If we assume the interaction potential is uniform in k, or $V_{kk'} = V_0$ for all values of k. Then equation 1.3 simplifies to

$$1 \simeq V_0 D(E_F) \int_{-\omega_D}^{\omega_D} d\xi \frac{\tanh \frac{\beta}{2} \sqrt{\xi^2 + \Delta_0^2}}{2\sqrt{\xi^2 + \Delta_0^2}} \tag{1.4}$$

The gap equation can then be solved to determine the energy gap Δ_0 for forming Cooper pairs. In conventional superconductors, the gap is isotropic in k. This attraction is caused by electron-phonon coupling. The strength of the coupling comes from the ions, and this has been experimentally confirmed through the isotope effect, where the phonon strength was modulated by using different isotopes in the superconductor.

BCS theory makes predictions about the critical temperature, specific heat, and superconducting gap. In the weak coupling limit, these quantities agree well with conventional superconductors. However, they fail when applied to various high temperature superconductors, in particular the cuprates. These HTS's, termed for their high T_C compared to conventional superconductors, launched a renewed quest to unravel alternate microscopic mechanisms of superconductivity.

In general, an unconventional superconductor is defined to be one with an order parameter with lower symmetry than the underlying lattice. To understand unconventional superconductors, we return to the gap equation obtained from the BCS Hamiltonian. This equation applies to interactions scattering electrons from k to k'. In the case of a strong interaction between neighbors, the potential $V_{kk'}$ is not necessarily constant. Alternate interaction potentials can be applied, such as

$$V_{kk'} = 2V_1[\cos(k_x - k'_x)a + \cos(k_y - k'_y)a], \tag{1.5}$$

which describes a nearest neighbor interaction on a square lattice. In the case $V_1 < 0$, this potential is most attractive at $k - k' = 0$ and most repulsive when $k - k' = \pi/a$. Such a potential would be favorable for superconductivity. The scattering by a vector $Q \approx (\pi/a, \pi/a)$. The gap equation allows for such a potential if Δ_k also changes sign. In the cuprates, this is an alternating sign in the gap, which changes sign along the diagonals of the Brillouin zone. This is *d-wave* pairing. One finds a gap that satisfies the symmetries takes the form

$$\Delta_k = \Delta_0(\cos(k_x a) - \cos(k_y a). \tag{1.6}$$

1.2.1 Hubbard model

The Hubbard model is a toy model that describes the underlying physics of the d-wave superconductivity. The Hubbard Hamiltonian is

$$H = -\sum_{ij\sigma} t_{ij} c^\dagger_{i\sigma} c_{j\sigma} + U \sum_i c^\dagger_{i\uparrow} c_{j\uparrow} c^\dagger_{i\downarrow} c_{j\downarrow}, \tag{1.7}$$

where t is the hopping between nearest-neighbors and U is an on-site repulsion term. For $U = 0$, the model consists of a lattice that is noninteracting. As U is increased, the increasing on-site repulsion leads to a balance that favors pairing. In undoped cuprates, there is an average of one electron per unit cell, which leads to a half filled band in the single-particle picture. For strong U, this leads to the Mott insulator state, with one electron on every site. The electrons are localized due to the repulsive interaction, in contrast to trivial insulators with a filled band. With small levels of doping, it is possible to free some of these carriers to induce conductivity.

1.2.2 Mott insulators

Mott insulators are of interest due to their proximity to high temperature superconductivity. Generally insulators have rapidly increasing resistivity with decreasing temperature. In certain cases the electrons can exhibit variable range hopping (VRH) [27]. This is caused by hopping between randomly distributed sites, and the resistivity takes the form

$$\rho_{VRH}(T) = A \exp{(T_0/T)^\alpha}. \tag{1.8}$$

In cuprates, this state is also antiferromagnetic, as the single spins on a square lattice adopt alternating orientations. However, the Mott insulating phase may extend to other electronic phases where the conduction becomes suppressed due to localization from Coulomb interac-

tions.

One candidate Mott insulator is $1T$-TaS_2, a TMD with a CDW phase. At 350 K, there is a transition into an incommensurate CDW, followed by a commensurate CDW at 200 K. This structure is a $\sqrt{13} \times \sqrt{13}$ supercell with the Ta atoms clustering into a star of David formation. $1T$-TaS_2 is predicted to be a metal in single particle band theory, which suggests the insulating behavior observed is due to a Mott insulator phase. It is a candidate quantum spin liquid [28]. Unlike the Mott insulators in cuprates, $1T-TaS_2$ does not have apparent magnetic order. The lack of order is thought to be caused by a Z_2 gapped spin liquid. Pressure studies have found a transition from the CDW to a superconducting state. Chemical doping is also a potential pathway to superconductivity out of the Mott insulator phase.

1.2.3 Triplet superconductivity

Another form of superconductivity with a nonuniform gap belong to the class of triplet superconductors. The general gap function can be expressed as a 2×2 complex matrix

$$\overline{\Delta_{\vec{k}}} = \begin{pmatrix} \Delta_{\vec{k},\uparrow\uparrow} & \Delta_{\vec{k},\uparrow\downarrow} \\ \Delta_{\vec{k},\downarrow\uparrow} & \Delta_{\vec{k},\downarrow\downarrow} \end{pmatrix}. \tag{1.9}$$

The components of this matrix are related to the wavefunction ψ of the Cooper pairs. Since the Cooper pairs are bosons, the overall wavefunction is even. This imposes constraints on the allowed spin and orbital components of ψ; an even orbital function must have a spin singlet state, while an odd orbital function must have a spin triplet state. This also implies

$$\overline{\Delta_{\vec{k}}} = -\overline{\Delta^T_{-\vec{k}}}. \tag{1.10}$$

The matrix in Equation 1.9 can then be expressed in the form

$$\overline{\Delta_{\vec{k}}} = \begin{pmatrix} -d_x(\vec{k}) + id_y(\vec{k}) & \psi(\vec{k}) + d_z(\vec{k}) \\ -\psi(\vec{k}) + d_z(\vec{k}) & d_x(\vec{k}) + id_y(\vec{k}) \end{pmatrix} = i\sigma_y(\psi(\vec{k}) + \vec{d}(\vec{k}) \cdot \vec{\sigma}). \tag{1.11}$$

In the case of conventional pairing, the gap function is constant, and $\Delta_{\vec{k}} = \Delta_0$. However, in other superconducting states the pairing may be anisotropic with nonzero $\vec{d}$, such as

$$\vec{d}(\vec{k}) \propto \hat{z}(k_x \pm ik_y), \tag{1.12}$$

in which case the gap has nodes when $k_x = k_y = 0$. This is a p-wave state. In materials with strong ferromagnetic interactions, spins are likely to align in parallel orientation, which favors a spin-triplet state. This can be distinguished in practice with a measurement of the spin susceptibility; the spin susceptibility of a spin singlet superconductor goes to zero as temperature decreases, but it remains finite in the triplet cases. The magnetic field no longer needs to break the Cooper pairs to align the spins. Superconductors such as Sr_2RuO_4 are believed to have a gap with p-wave symmetry.

Superconductors with p-wave order parameters are interesting for several reasons. Some of the pairing symmetries are topologically non-trivial and support edge modes. Superconductors with p-wave pairing are predicted to host topological edge states with Majorana fermions. These quasiparticle excitations obey non-Abelian statistics and may be applicable to quantum computation [29][30][31].

1.3 Transition metal dichalcogenides

There are many members in the family of TMD materials. Each one is host to a diverse set of phenomena that is a consequence of its chemical composition, crystal structure, and thickness. They have been a versatile platform for realizing superlattice structures and studying correlated phenomena. This makes TMD-based compounds a target for studying unconventional superconducting phases. Here, we discuss several of the members explored in this thesis.

1T-VS_2 is a metallic TMD with one monolayer in every unit cell. It contains S atoms arranged in an octahedral coordination about the V atom. *1T*-VS_2 is predicted to host a charge density wave (CDW) phase in the monolayer limit[32]. It has been suggested VS_2 has a tunable ferromagnetic phase in the monolayer[33]. The crystal is typically synthesized under high pressure or through Li de-intercalation of $LiVS_2$ [34]. This makes it difficult to isolate monolayers of VS_2 , where the instability towards a CDW is strongest.

NbS_2 is a metal with two layers in every unit cell. It occurs naturally in the *2H* polytype, which has local broken inversion symmetry. *2H*-NbS_2 is a superconductor with a T_C of 5.8 K in the bulk, dropping to 2.1 K in the few-layer limit [35]. This decrease in T_C is attributed to a decrease in the electron-phonon coupling as the number of layers decreases. Unlike many of the other Group V TMDs, NbS_2 lacks a CDW transition. It has been intercalated with Cr atoms to realize a chiral helimagnet [36] and with Fe to realize antiferromagnetic order

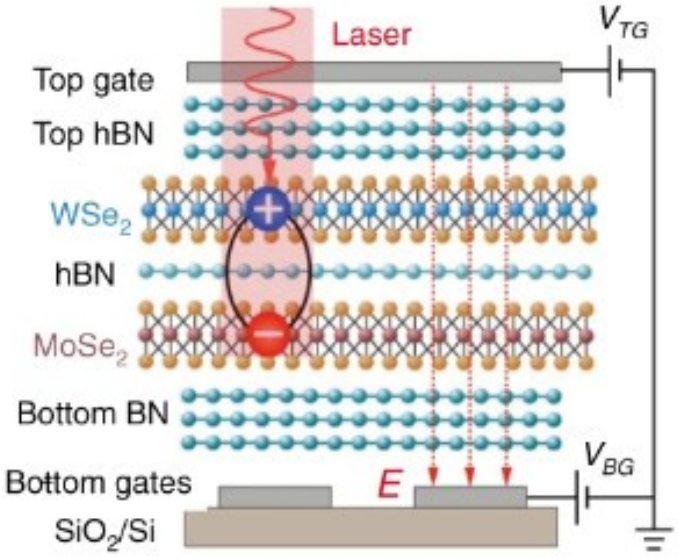

Figure 1.3: Exciton physics in $MoSe_2$ and WSe_2 heterostructures. Adapted from [42].

[37].

MoS_2 is a semiconductor with two layers in the unit cell arranged in the *2H* polytype. In the monolayer, it changes from an indirect bandgap to a direct bandgap semicondcutor. Furthermore, strong spin-orbit coupling (SOC) splits the bands at the K and K' points in the Brillouin zone. This creates spin polarization in each valley, which can be probed and manipulated optically. This has led to proposed applications in spintronics. MoS_2 has also been a platform for the observation of exciton physics. In bulk *2H*-MoS_2, pressure reduces the bandgap of the semiconductor, and near the semimetal regime MoS_2 is predicted to have an exciton instability that leads to an excitonic insulator state [38]. Excitons are found in few-layer heterostructures and can be classified as intralayer or interlayer excitons based on the physical location of the electron and hole [39]. Interlayer excitons attracted interest because of their relatively long lifetime enabled by the real-space separation. They may be manipulated with electric fields due to their electric dipole moment. Excitons in bilayer heterostructures can condense to form an exciton insulator phase. This bosonic phase of matter is interesting because it hosts a charge-neutral supercurrent and is tunable a platform for studying the BEC-BCS crossover.

Monolayer MoS_2 and WS_2 have both been incorporated in field effect transistors (FETs) [40]. They have been synthesized at wafer scale [41] and incorporated into various circuits for logic operators or inverters, making them candidates for components in larger integrated circuits.

MoS_2 applications are limited in part by disorder, either due to intrinsic defects like sulfur vacancies or extrinsic ones such as surface charge impurities [43]. Advances in materials science and nanofabrication have led to some reductions in disorder. Hexagonal boron nitride (hBN) substrate encapsulation reduces disorder by covering the surface of the TMD with an insulator that is also atomically flat. hBN removes charge inhomogeneities in graphene, enabling observations of the ordinary and fractional quantum Hall effect [44][45]. Similar encapsulation for MoS_2 and other semiconducting TMDs lead to higher mobilities and enhanced photoluminescence [46]. The degree of improvement is not as large as in graphene, as TMDs have a lower energy for defect formation. New synthesis methods to decrease intrinsic disorder in TMD materials is a subject of great interest to physicists and engineers alike.

1.4 Misfit superlattices

Misfit superlattices are a TMD superlattices formed from the intercalation of rock salt layers or organic molecules between the TMD layers. These crystals are termed misfits because the intercalated layer belongs to a different crystal lattice family than that of the TMD. This results in *e.g.* an axis with incommensurate lattice vectors. For example, the $(SnS)_{1.17}NbS_2$ is a rock salt misfit, where the SnS layer belongs to an orthorhombic unit cell, in contrast to the hexagonal unit cell of the TMD layer [47][48]. This incommensurate modulation and weak interlayer coupling lends itself to a variety of electronic, structural, and thermodynamic properties that are interesting for fundamental physics and industrial applications. For example, misfit compounds host CDWs and superconductivity. They are proposed for use as thermoelectrics due to the potential quenching of thermal conductivity [49]. Misfit compounds serve as platforms for intercalation of other compounds.

With misfit compounds, it is possible to stabilize a variety of TMD superlattices, including various polytypes of the TMD layer [50]. The spacer layer can also be varied chemically to tune the interfacial properties of the rock salt layer or realize different incommensurate lattices. This large flexibility can also be undesirable, as the compounds are prone to structural and chemical disorder. This can be a limitation to the electronic quality achievable in misfit superlattices. Nonetheless, they are interesting counterparts to the TMD superlattices studied in this thesis.

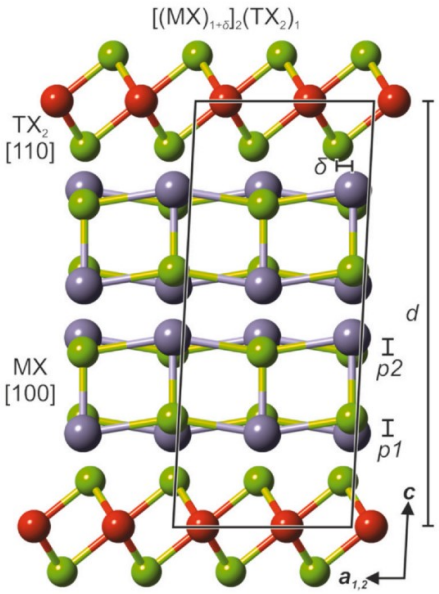

Figure 1.4: Structure of misfit compound $[(MX)_{1+\delta}]_2(TX_2)$, where $(MX)_{1+\delta}$ is a orthorhombic rock salt structure and TX_2 is a hexagonal TMD layer. Adapted from [50]

1.5 Natural superlattice $Ba_6Nb_{11}S_{28}$

As described above, $Ba_6Nb_{11}S_{28}$ is a superlattice with a 2D superconducting phase originating from the TMD 2H-NbS_2 layers. The superconductivity is anisotropic owing to the layered nature of the crystals. The long mean free path relative to coherence length of the quasiparticles indicates the cleanliness of the 2D superconductivity. The Fermi surface can be modeled as that of 2H-NbS_2 with zone-folding from the 3×3 superstructure of the Ba_3NbS_5 layer. This is supported by transmission electron microscopy (TEM) and quantum oscillations measured in transport. The presence of quantum oscillations also indicates a high mobility exceeding that of bulk $2H$-NbS_2 [24]. The superconductivity exceeds the Pauli limit in H_{c2}. There is evidence for an FFLO phase from torque magnetometry, which shows a sharp decrease in diamagnetism near H_{c2} [25]. This phase is suggested to be a spatially modulated superconducting phase in which the Cooper pairs have a nonzero momentum. The FF state consists of Cooper pairs with momentum $\Delta \propto e^{iQ\cdot R}$, while the LO state consists of the Cooper pairs with $\Delta \propto \cos(Q \cdot R)$. The crystals of $Ba_6Nb_{11}S_{28}$ may be exfoliated, which opens the possibility of examining these phenomena as a function of carrier doping.

The discovery of a natural, commensurate crystal with encapsulated TMD layers further suggests the existence of other variants. By varying the chemical composition of the constituent TMD, it may be possible to access the monolayer electronic properties of other

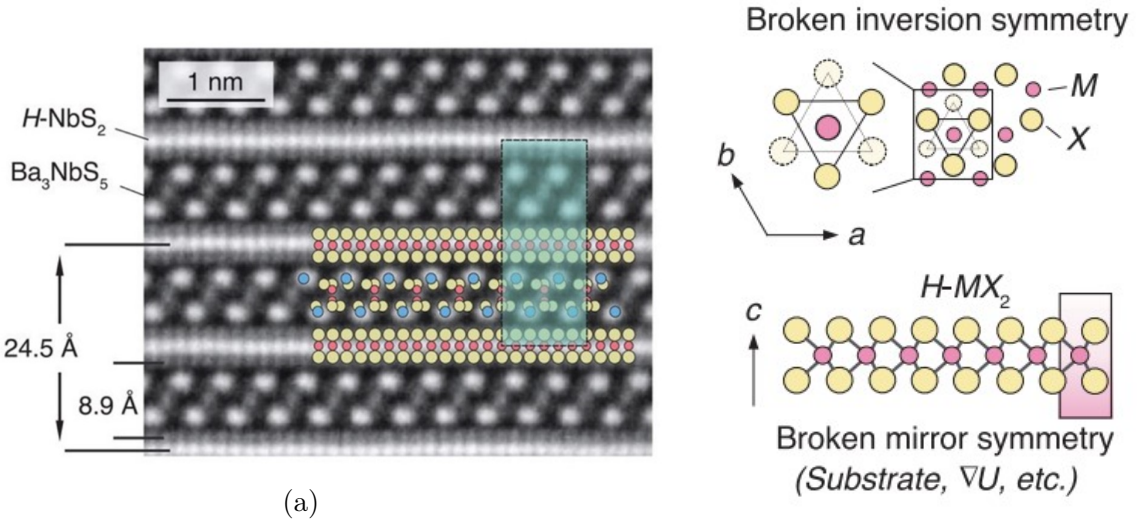

(a) (b)

Figure 1.5: Structure of a natural TMD superlattice $Ba_6Nb_{11}S_{28}$: (a) Cross sectional TEM. (b) Crystal structure along the *ab*-plane and *c*-axis displaying symmetries of monolayer *2H*-NbS_2. Adapted from [24].

TMDs in a natural bulk crystal. By controlling the composition of the spacer, we can also tune the properties of the TMD through interfacial interactions. In the following chapters, we discuss the superlattices synthesized from these natural TMDs and their relation to the materials discussed here.

Chapter 2

Experimental Methods

In this chapter, we describe the experimental techniques utilized in this thesis. The workflow for the materials presented begins with crystal synthesis. Following synthesis, we analyze the physical structure through diffraction. Once this has been established, we then characterize the electronic properties through transport measurements. Other forms of characterization are applied as necessary for the understanding of the material.

2.1 Crystal synthesis

Single crystals of Sr-VS_2 were synthesized through a solid-state reaction of SrS, S, and V in a 1:1:2 ratio. This is combined with $SrCl_3$ in a 9:1 mass ratio. All precursor materials were obtained from Alfa Aesar and of 99.99% purity or higher. SrS, V, and $SrCl_3$ came in the form of powder, while S came in pellets, all stored in an inert atmosphere in a glovebox. The mixture was prepared in the glovebox, mixed by mortar and pestle, and placed in an alumina crucible. The crucible was sealed in quartz ampoules under vacuum below 5×10^{-5} Torr. The sealed ampoule was placed in a furnace that was heated to 950 °C in 24 hours. After holding at that temperature for five days, the furnace was cooled at 2 °C/hr to 750 °C, after which the furnace was cooled to room temperature over 24 hours. A representative growth sequence is shown in Figure 2.1. Other superlattice compounds were synthesized by varying the initial compounds and stoichiometry. Additional crystals were grown either by substitution of the transition metal elements, such as Nb instead of V, or substitution of the alkaline earth metal.

Single crystals can be mechanically separated from the product and are dark grey to black in color. They have a slight luster on are quasi-two-dimensional in appearance. The size of the single crystals are up to 0.5 mm × 0.5 mm × 50 μm in size. The crystals appear as platelets with hexagonal facets. The crystals are stable in air and do not show signs of

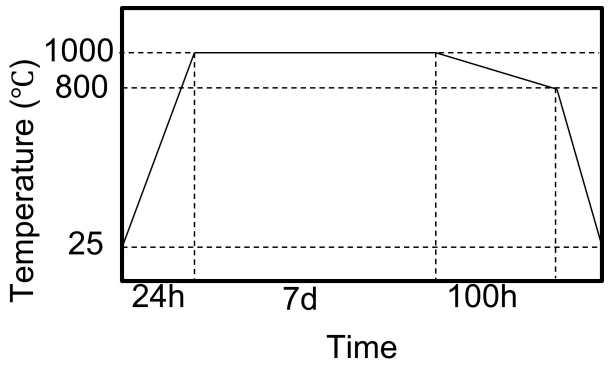

Figure 2.1: Typical growth sequence of superlattice compounds

degradation over several hours. Crystals can be cleaned with mechanical exfoliation by tape.

Chemical vapor transport (CVT) was used for the crystal growth of some crystals investigated in this thesis. The process involves a reaction in a pressurized tube furnace which allows the deposition of gaseous precursors. There is a temperature gradient applied to control the flow of the precursor material in the presence of a transport agent such as I_2. The material deposits in the nucleation area as they are transported. This technique is readily utilized to grow large single crystals of TMDs. For the growths in this thesis, I_2 was used as the transport agent.

2.2 Structural characterization

To characterize the structure of the synthesized compounds, we perform X-ray diffraction (XRD) and transmission electron microscopy (TEM). For powder XRD (PXRD), crystals were ground by a mortar and pestle to a fine powder. This powder was then uniformly distributed on a zero-background silicon plate. The X-rays were collected in the Bragg-Brentano geometry on a Panalytical Xpert multipurpose diffractometer with a copper source. The collected patterns were analyzed in Highscore Plus. Single crystal diffraction is performed on a Bruker D8 General Area Detector Diffraction System (GADDS) with a cobalt source.

The samples for TEM are prepared by focused ion beam (FIB) in the FIB-SEM VELION at MIT.nano. A single crystal was mounted on carbon tape along the crystallographic axis to be imaged. The FIB milled the sample with Au ions to cut out a cross-sectional lamella of dimensions 1 µm x 5 µm. Finally, the lamella is lifted out and polished down to electron transparency.

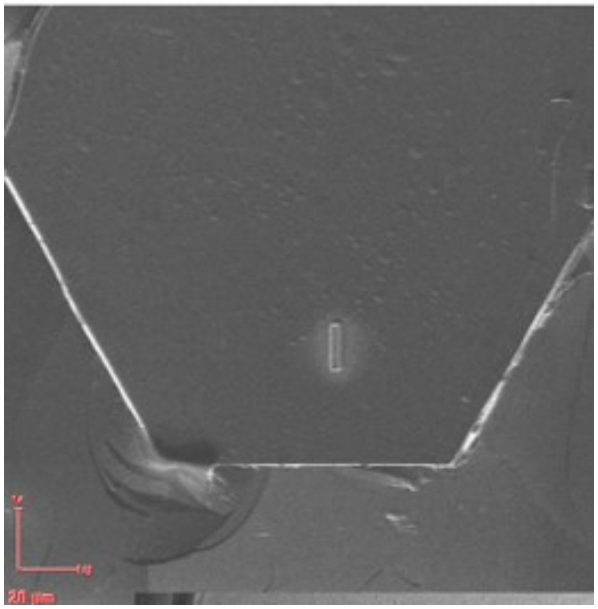

Figure 2.2: SEM image of sample surface with lamella removed via FIB.

Dr. Kent Jingxu Zheng performed TEM imaging on the samples in this work. The lamella was loaded into the Themis Z TEM at MIT.nano and imaged in high-angle annular dark-field imaging (HAADF) for cross-sectional real space images. The lamella was aligned in the TEM along a high symmetry axis, identified by the increase in contrast of the Bragg peaks. Selected-area electron diffraction (SAED) was performed once the lamella was aligned.

2.3 Electric transport measurements

The electronic properties of the crystals in this thesis were characterized by electronic transport experiments. A current is applied across the crystal creates an electric field,

$$\vec{J} = \bar{\sigma}\vec{E}, \tag{2.1}$$

where $\vec{J}$ is the current, $\bar{\sigma}$ is the conductivity tensor, and $\vec{E}$ is the electric field. The conductivity is in turn related to resistivity by

$$\bar{\rho} = \bar{\sigma}^{-1}. \tag{2.2}$$

In all transport measurements in our experiments, a voltage is recorded, which can then be converted to electric field.

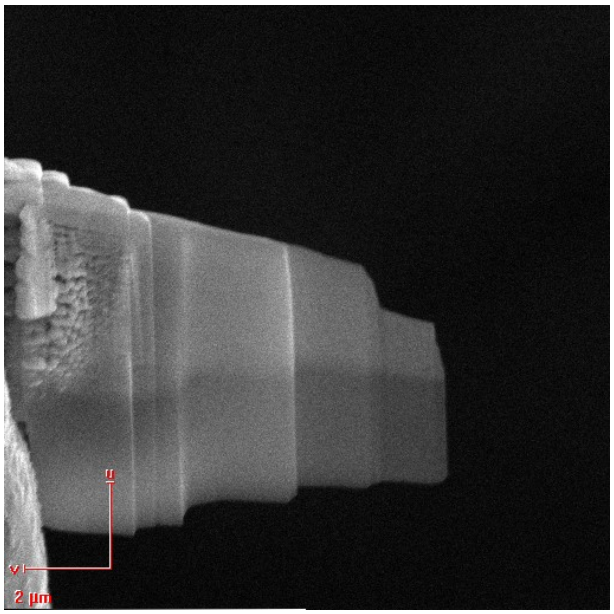

Figure 2.3: SEM image of TEM lamella prepared by FIB.

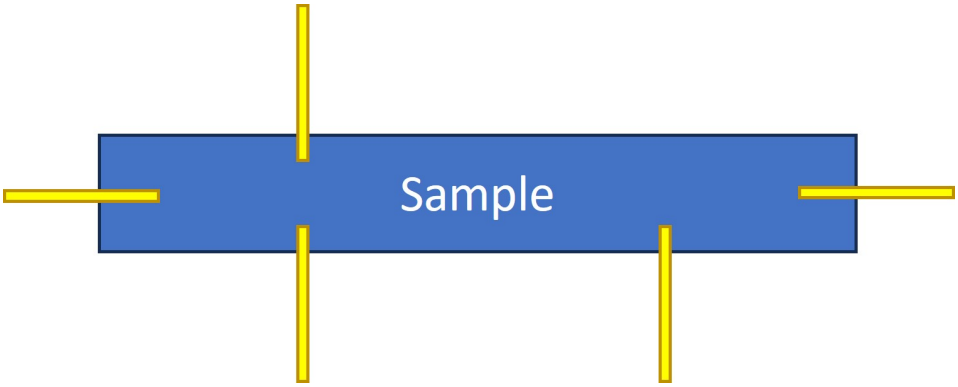

Figure 2.4: Wiring schematic for a five-point geometry.

The conventional method to measure the resistivity tensor is through a five point contact setup. In a rectangular sample, the contacts can be arranged as shown in Figure 2.4. The current is flowed across wires on opposite ends of the sample, and the longitudinal voltage is measured across leads aligned in a collinear fashion. For the Hall resistance, the voltage is measured across two transverse leads. The resistance in the crystal can be converted to resistivity by measuring the dimensions. In practice, not all samples are rectangular in shape, and the voltage contacts are not aligned in perfect longitudinal or transverse direction, leading to mixing of the resistivity components in the signal. The components can be separated under an applied magnetic field, since ρ_{xx} (and diagonal terms) is symmetric

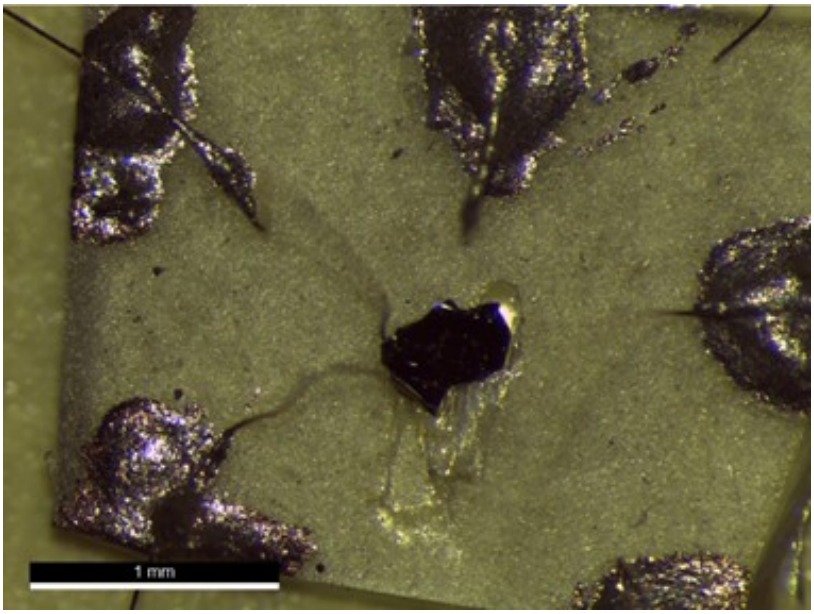

Figure 2.5: Sample with a five-point geometry wired for transport measurements.

while ρ_{xy} is anti-symmetric. This is expressed as

$$\rho_{xx} = \frac{1}{2}(\rho(B) + \rho(-B)), \tag{2.3}$$

and

$$\rho_{xy} = \frac{1}{2}(\rho(B) - \rho(-B)). \tag{2.4}$$

To make physical contacts, gold wires were attached to sapphire substrates with conductive silver epoxy (Epotek H20E) in a five-point geometry. Single crystals were then mounted on sapphire substrates and fixed in place with GE varnish, an insulating adhesive that is stable down to cryogenic temperatures. Silver paste (Dupont Ag paint) was used to connect the gold wire contacts to the crystal. The conductive paints and wires are intended to minimize the resistance between the sample and measurement instrument, while providing a robust connection down to cryogenic temperatures. In-house measurements are made with an SRS 860 lock-in amplifier with an AC excitation current on a CS 580 voltage-controlled current source. Typical excitations were applied with frequencies up to 60 Hz and amplitudes below 1 mA to mitigate sample heating.

The majority of measurements are done with an AC current excitation to reduce noise that occur at low frequencies. In addition, it filters out any parasitic frequencies that may be picked up in a DC measurement. The Keithley 6221 (or CS 580) outputs a current of the

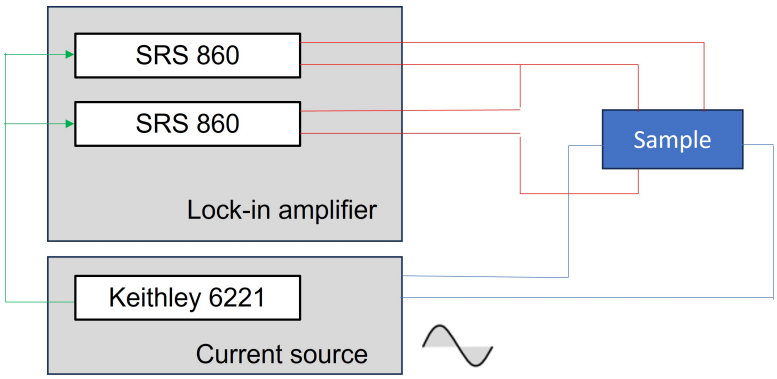

Figure 2.6: Schematic of electronics setup for a five-point measurement.

form

$$I = I_0 \cos(\omega t + \phi), \tag{2.5}$$

where ω is the angular frequency and ϕ is a phase shift. This is synchronized with the lock-in amplifier with a reference, typically a square wave at the same frequency, as shown in Figure 2.7. The lock-in multiplies the signal with its own lock-in reference generated from the reference, which results in a product of sine waves

$$V_{psd} = \frac{1}{2} V_{\text{sig}} V_L \Big[\cos([\omega_r + \omega_L]t + \theta_{\text{sig}} + \theta_{\text{ref}}) + \cos([\omega_r - \omega_L]t + \theta_{\text{sig}} - \theta_{\text{ref}}) \Big]. \tag{2.6}$$

If the two frequencies are matched, $\omega_r = \omega_L$, then there will be a DC signal with the amplitude of the sample response. In addition, the phase offset can be matched by adjusting θ_{ref} to match θ_{sig}. This can also be done by performing a second multiplication with another reference signal. This process is known as phase-sensitive detection (PSD), and it enables low noise measurements. This is critical in many experiments, where the sample response may be small and where there are many sources of electronic noise in the sample environment. This technique can be applied to a general periodic signal; the measured response will be the fundamental Fourier component of the periodic signal.

An alternative measurement scheme is tp perform "Delta mode" measurements of resistance and I-V characteristics using a Keithley 2182A nanovoltmeter and Keithley 6221. In this setup, the nanovoltmeter is connected to the current source to trigger on square current pulses from the current source and measure the voltage response. The voltage signal is averaged over several square pulses. The duration of the pulses are kept short to minimize low-frequency noise and reduce heating effects. The pulses were 0.5 ms in width with amplitude of 10 µA. For I-V measurements, the amplitude of the current pulses was stepped

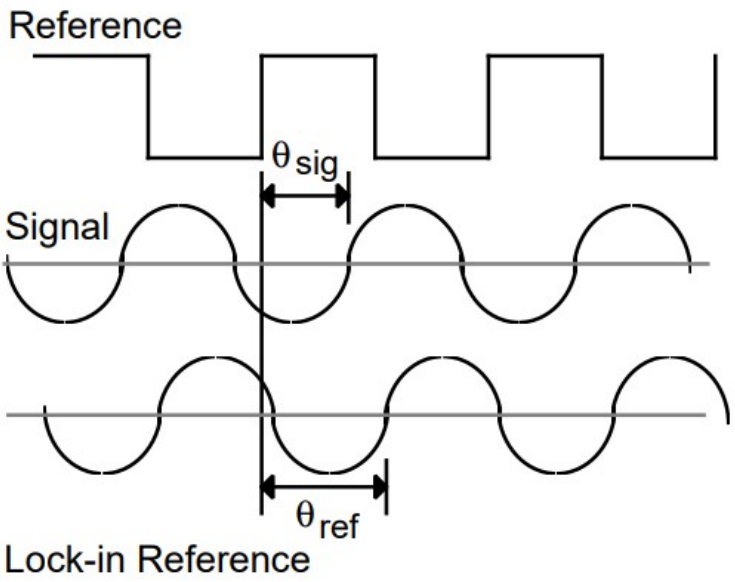

Figure 2.7: Lock-in signal from the current source. Adapted from [51].

sequentially up to 0.5 mA.

Several measurements were completed at the DC Field facility at the National High Field Magnetic Laboratory in Tallahassee, Florida. Transport and torque magnetometry measurements were carried out at Cell 6 and Cell 9, which host resistive magnets with magnetic fields up to 41.5 and 32 Tesla respectively. The samples were loaded in a He-3 cryostat.

The cryostat consists of a 16-pin chip carrier that is mounted at the end of a probe. The samples are mounted on a platform connected to a string rotator equipped with a Hall sensor and cernox thermometer. The temperature is monitored and controlled with Lakeshore 372 temperature controllers. The probe is inserted into a liquid He-4 cryostat, which is controlled by a 1K pot and sorb.

In a magnetic field, ground loops in the electronic setup can create an induced flux through the loop, which creates artificial noise in the measurement. To reduce noise, all instruments were connected to clean ground through a single port. Twisted pairs of wires were made between the electronics and sample platform to minimize current loops.

2.3.1 Pressure Cell measurements

In experiments on Sr-VS_2, the transport devices are set up in an HPC-33 hydrostatic pressure cell by Quantum Design to study the resistivity as a function of pressure. The contacts

Figure 2.8: Setup of hydrostatic pressure cell. Adapted from [52].

are prepared in the four-contact geometry as described above and then placed in a piston cell filled with an inert pressure medium. A hydraulic press enables transport measurements up to nearly 3 GPa. The applied pressure is tracked by a Sn manometer, which has a superconducting temperature sensitive to change.

In collaboration with Stan Tozer and Audrey Grockowiak from the National High Field Magnet Laboratory, a diamond anvil cell (DAC) was prepared with a crystal of Sr-VS_2. The diamonds were prepared with an SS304 gasket and Nujol oil as a pressure medium. The wires used for contacts to the sample in the DAC were 0.0007 in. PtIr wire. The wires are 10 - 20 µm wide. The pressure applied to the DAC range up to 7.6 GPa. The resistance of the wire was 1 Ω/mm. Four contacts were made to the crystal. In some cases two-point measurements were performed in a pulsed configuration.

2.4 Torque Magnetometry

We performed torque magnetometry to understand the magnetic properties of the synthesized crystals [53]. The piezocantilevers used here were SCL-Sensor Tech cantilevers. Single crystals were mounted on piezocantilevers with small amounts of vacuum grease (Dow Corning). The vacuum grease freeze and attaches the sample to the cantilever. The crystals are balanced on the tip of the cantilever, with care taken to mount the crystal away from the sensors. This allows the cantilever to oscillate without significant damping.

When a magnetic field is applied, the magnetization in the crystal creates a torque according to

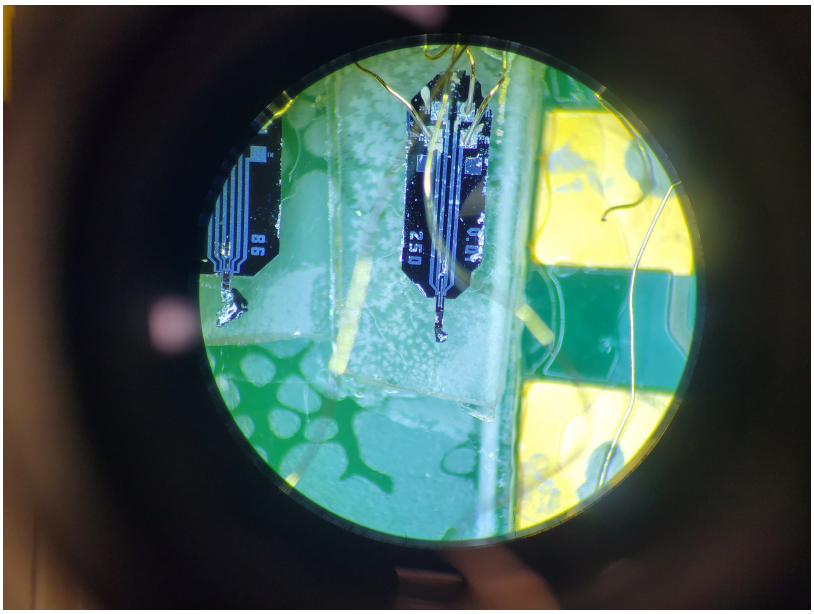

Figure 2.9: Cantilever with crystal mounted for torque magnetometry.

$$\tau = M \times H, \tag{2.7}$$

which generates a voltage through the piezoelectric material. To measure the signal, the leads from the piezoelectric are connected in a Wheatstone bridge with two reference resistors. These serve to remove the magnetoresistance of the cantilevers at zero field. The output of the Wheatstone bridge is connected to a lock-in amplifier and preamplifier to record the torque response. For most experiments, we used an SRS 860 for the lock-in and an SR560 for the preamplifier.

From equation 2.7, the magnetic torque captures the perpendicular component of the magnetization, which can be used to extract the magnetic anisotropy. This measurement has been used to extract information on magnetic phases, de Haas van Alpha (dHvA) quantum oscillations, and diamagnetism from superconductivity. Depending on the application, the magnetic field must be applied at an angle relative to the cantilever in order to maximize the torque signal. The rotation axis of the cantilever is therefore aligned perpendicular to the magnetic field for the measurement.

Torque magnetometry measurements were made at the DC Field facility at the National High Field Magnetic Laboratory in Tallahassee, Florida and on the 65 T magnet at the Pulsed Field Laboratory in Los Alamos, New Mexico. The experimental setup at the Pulsed Field is similar to that at the DC field, except the magnet is pulsed.

2.5 Quantum oscillations

In a magnetic field, electrons in a metal undergo Landau quantization and form Landau levels (LL). As the field is varied, the levels pass through the Fermi surface and manifest as oscillations in physical quantities such as the resistance or magnetic susceptibility. The frequency and amplitude of the oscillations and give valuable insight into the Fermi surface of the material. Quantum oscillations are periodic in $1/B$, and their frequencies are related to the size of the Fermi pocket through

$$B_F = \frac{\hbar}{2\pi e} A_k, \tag{2.8}$$

where A_k is the area of the pocket perpendicular to B. By taking a Fourier transform of the magnetoresistance, the different frequencies may be extracted to obtain the pockets of the Fermi surface. Angle dependence of these frequencies can then map out the full 3D surface, a technique that has been employed to study a wide range of Fermi liquids ranging from elemental metals to the normal state of high temperature superconductors and topological materials.

The oscillations are damped by various factors including thermal broadening, scattering, and sample and magnetic field inhomogeneities. These factors are

$$R_T = \frac{2\pi^2 k_B T m^*}{\hbar e B} \sinh^{-1}\left(\frac{2\pi^2 k_B T m^*}{\hbar e B}\right) \tag{2.9}$$

and

$$R_D = \exp\left(-\frac{2\pi^2 k_B T_D m^*}{\hbar e B}\right). \tag{2.10}$$

These factors allow the extraction the effective mass of the quasiparticles in the pockets.

Chapter 3

Sr-VS_2 TMD superlattices

3.1 Synthesis and structural characterization

Initial growths of Sr-VS_2 were performed in a quartz tube in a catalyzed reaction outlined in Chapter 2. The crystals ranged in size from 50 to 500 µm in width and under 20 µm in height.

Further attempts for the growth were made in an alumina crucible. The crucible was sealed in a wider quartz tube, and the crucible was capped with a lid. Larger crystals were found between 500 μm and 1000 μm in width and 20 μm in thickness. The single crystals used for transport were chosen from these growths.

XRD patterns indicate the formation of a compound distinct from that of the precursors and VS_2. The strongest diffraction peaks match those of SrV_2S_5 along the c-axis. There are few peaks matched to reflections in the ab-plane. This difference in signal is likely due to the preferential orientation of the crystals. By fitting the measured peaks, we estimate the spacing along the c-axis to be 34 Å.

To understand the complex unit cell of Sr-VS_2, we prepared TEM lamellas with FIB from single crystals along different crystallographic directions. Dr. Kent Jingxu Zheng performed the TEM imaging for these lamellas. Along the [0001] direction, we observe a set of bright peaks arranged in a hexagonal pattern, which we associate with the Sr atoms, the heaviest atoms in the compound. Massive atoms produce reflections of stronger intensity.

Along the $[1\bar{1}00]$ direction, we observe the layered stacking of the TMD and spacer. The atoms in the spacer can be resolved, with the brightest atoms corresponding to the heaviest atoms. The spacer stacks in an ABC stacking pattern. The sulfur atoms in VS_2 are arranged in an octahedral coordination about the central vanadium, supported by the inversion center

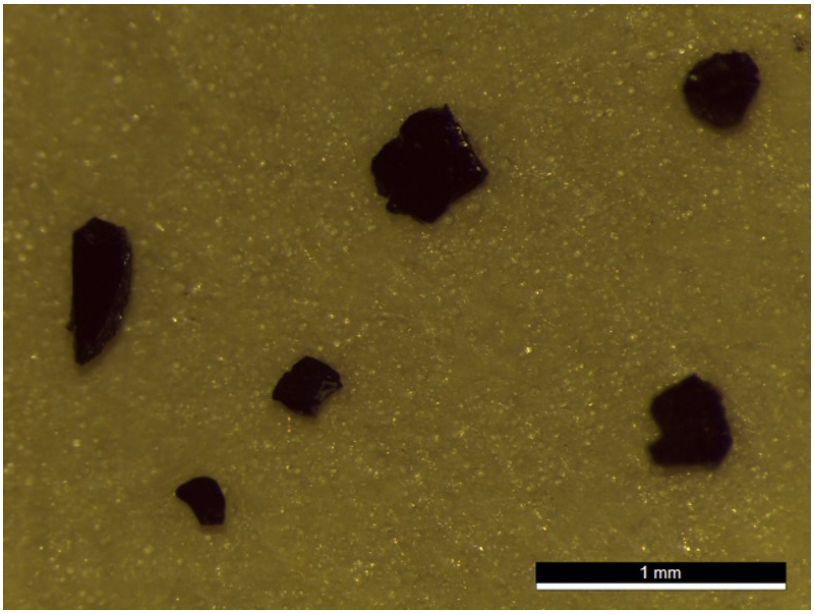

Figure 3.1: Single crystals of Sr-VS_2.

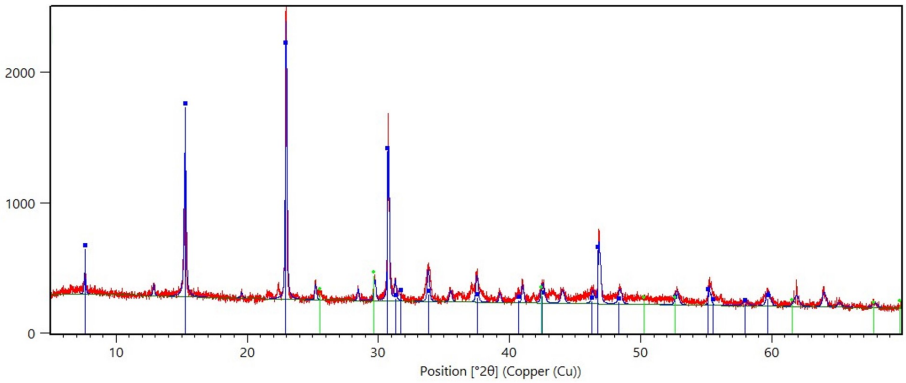

Figure 3.2: Powder X-ray diffraction of Sr-VS_2. Blue peaks are identified with the superlattice compound, while green peaks indicate trace amounts of SrS.

at each V atom.

The space group of the crystal structure is derived from the point group and Bravais lattice. We calculate the allowed symmetries to determine the point group of the system. The TEM images are transformed with each element in the point group and the intensities of the image are subtracted. The transformation is considered a symmetry if the subtracted intensity is negligible. The allowed symmetries are inversion and C_2 rotation, while reflections about [0001] and $[1\bar{1}00]$ are not. Since [0001] is a C_3 rotation axis, we can narrow the point group to C_3 or C_6. The allowed space groups are space groups 143 - 146 or 168 - 173.

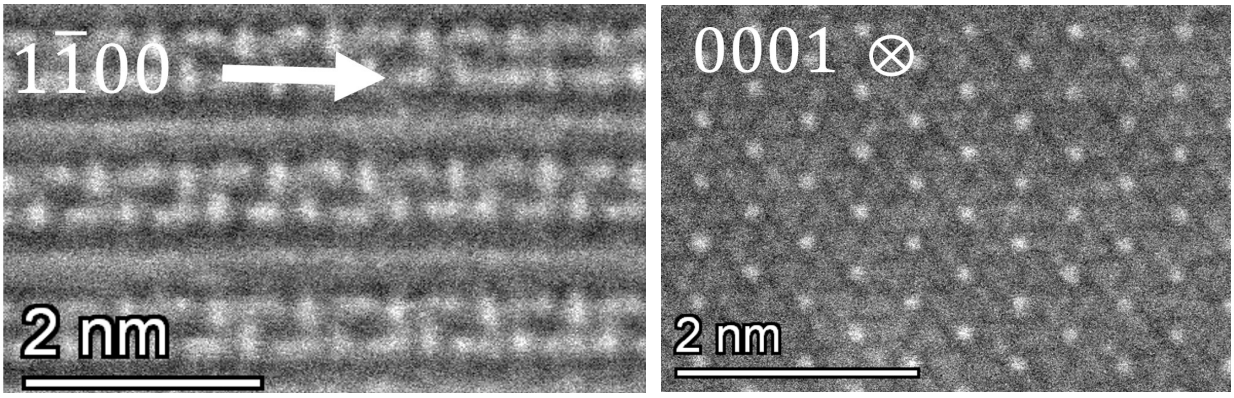

(a) (b)

Figure 3.3: (a) TEM Image of Sr-VS_2 along $[1\bar{1}00]$. (b) TEM Image of Sr-VS_2 along [0001].

Table 3.1: Chemical composition of Sr-VS_2 from EDX and XPS.

Atomic%	Sr	V	S
(EDX)	16.34	24.67	58.8
(XPS)	23.28	25.13	49.4

3.1.1 Chemical composition

The chemical composition of Sr-VS_2 was measured with electron dispersive spectroscopy (EDX) in SEM and X-ray photoemission spectroscropy (XPS). The results are shown in Table 3.1.

3.2 Transport

Next, we analyze the electronic properties of Sr-VS_2 through transport measurements. Figure 3.4 shows the longitudinal resistivity ρ_{xx} as a function of temperature. Sr-VS_2 is insulating, and the resistance increases by four orders of magnitude from 300 K to 1.8 K. We fit the transport data to an Arrhenius curve,

$$\rho_{xx} = A \exp(\frac{\Delta}{2k_B T}), \tag{3.1}$$

where Δ is the band gap in eV. From this fit in the temperature range 150 K to 300 K, we extract a band gap of 44 meV. The resistivity at 300 K is on the order of 10^{-6} Ω-cm. From band structure calculations in the literature [33], *1T*-VS_2 is a metal because its Fermi energy lies in the middle of a band. This raises the possibility that Sr-VS_2 is a Mott insulator. At temperatures below 10 K, the thermally activated hopping mechanism transitions to a

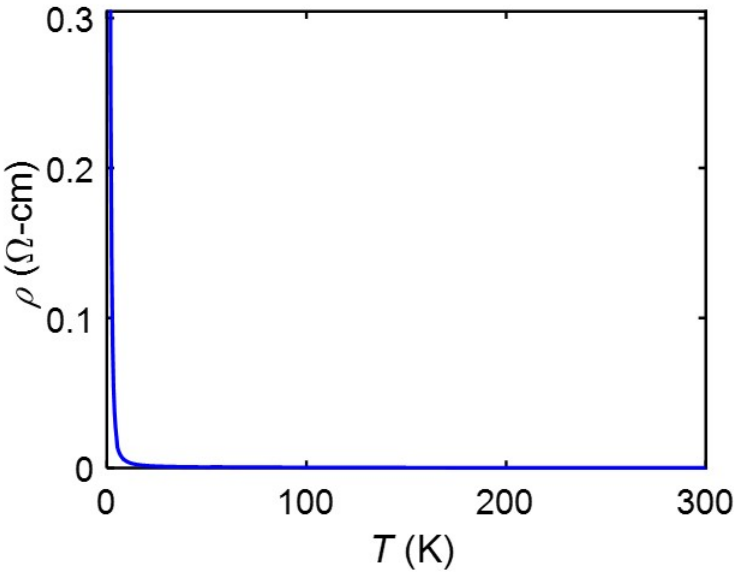

Figure 3.4: Longitudinal resistivity of Sr-VS_2 as a function of temperature.

variable range hopping, and the temperature dependence changes to

$$\rho_{xx} = A \exp(\frac{\Delta}{2k_B T})^{\frac{1}{d+1}}, \tag{3.2}$$

where d is the effective dimension of the carriers. A fit to this equation below 10 K results in an exponent of 1/3, shown in Figure 3.5. This type of transport is consistent with VRH describing 2D conduction.

3.2.1 Comparison with misfit compounds

In VS_2 synthesized under high pressures, the resistivity of powder samples show an increase as temperature decreases, consistent with non-metallic behavior. In addition, optical conductivity measurements find an absence of a Drude peak, which also suggests the electrons are localized though impurities or interactions. Variable range hopping in the misfit compound $(LaS)_{1.196}(VS_2)$ has also been ascribed to Mott insulating behavior [54]. Single crystals of $(LaS)_{1.196}(VS_2)$ have exhibited insulating behavior that can be fit to a power law for variable range hopping. The conductivity can be switched with a strong current that causes dielectric breakdown and results in nonlinear $I - V$ characteristics [55]. A chemical doping series on the lanthanum site with different alkaline earth metals shows a decrease in resistivity [56]. Angle resolved photoemission (ARPES) revealed a nearly filled band, and diffraction measurements reveal structural distortions in the vanadium atoms that lead to the localization.

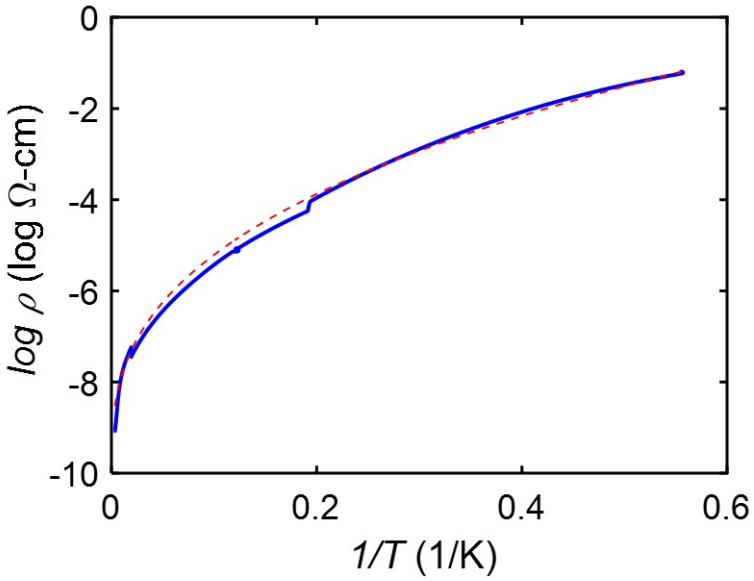

Figure 3.5: Variable range hopping conduction in Sr-VS_2. The resistance is shown in blue, and the VRH fit to the data is shown in red.

In contrast, photoemission measurements of the sister misfit compound $La_{(1.17-x)}Pb_x(V)_{3.17}$ have shown evidence for Mott-Hubbard behavior. The similar electronic properties of the VS_2-based compounds suggest the possibility of a correlated system. Raman spectroscopy on Sr-VS_2 may provide insight on the mechanism that governs the localization.

3.2.2 Magnetoresistance and Hall effect

Figure 3.7 shows the magnetoresistance (MR),

$$MR = \frac{\rho(H) - \rho(0)}{\rho(0)}, \tag{3.3}$$

at several temperatures. There is a marked positive MR at 2 K which this diminishes rapidly as temperature increases. The MR increases up to 60% of its zero-field value at 9 Tesla. The field-dependent data are sample dependent, with some samples exhibiting 80% MR.
In a single-band metal, the carriers in the crystal undergo scattering in a magnetic field that scales quadratically with field and increases with the mobility of the sample. While Sr-VS_2 is likely not a simple metal, we use can perform this analysis to quantify and consider the MR response. The mobility can be calculated as

$$MR = \mu_{MR}^2(\mu_0 H)^2, \tag{3.4}$$

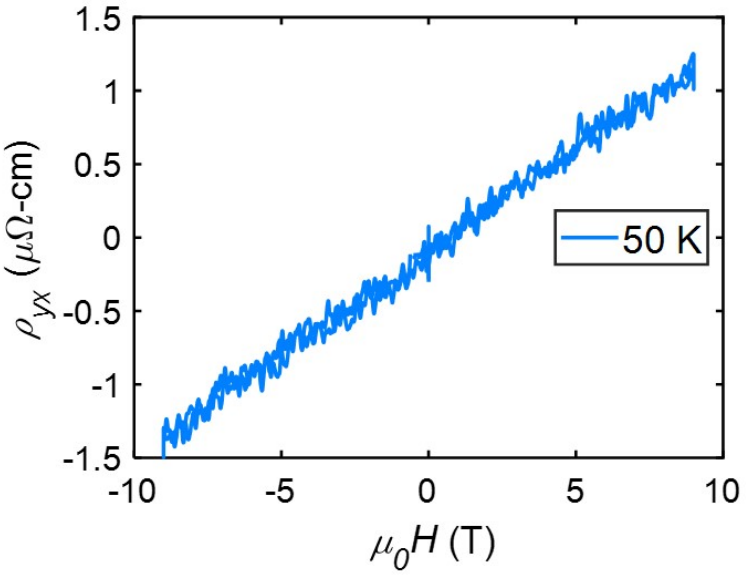

Figure 3.6: Hall effect in Sr-VS_2.

from which we can calculate the mobility $\mu_{MR} = 0.838 \frac{\text{cm}^2}{\text{V·s}}$ at 1.8 K. Further work is needed to determine the origin of magnetoresistance here.

Figure 3.6 shows the ρ_{yx} component of resistivity measured as a function of magnetic field. The Hall coefficient can be calculated as

$$R_H = \frac{E_y}{j_x B_z} = \frac{\rho_{yx}}{B_z}, \tag{3.5}$$

where E_y is the electric field created by the measured Hall voltage, j_x is the applied current density, and B_z is the magnetic field. The Hall coefficient is $4 \times 10^{-8} \Omega$m/T at 50 K. With the Hall coefficient, we can calculate the carrier density of the material

$$R_H = \frac{1}{ne}, \tag{3.6}$$

where n is the carrier density and e is the electron charge. For typical metals, the carrier density ranges from 10^{22} to 10^{23} cm^{-3}, while for semiconductors that value is below 10^{18} cm^{-3}. The carrier density in Sr-VS_2 is 3×10^{19} cm^{-3}.

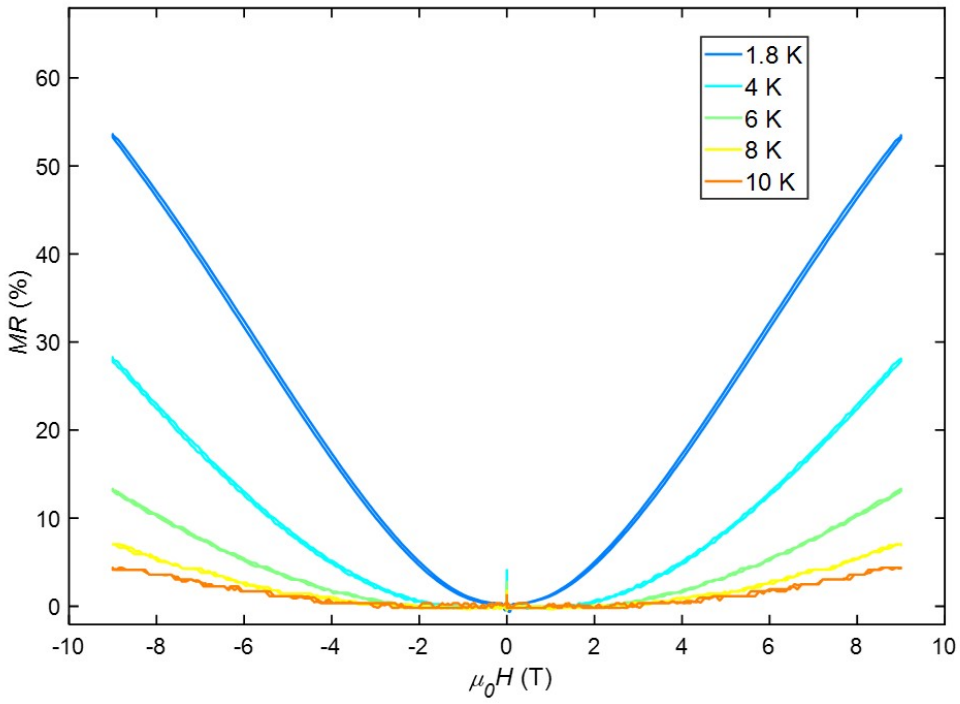

Figure 3.7: Magnetoresistance in Sr-VS_2.

3.2.3 Pressure cell measurements

To test the possibility of an insulator-metal transition in Sr-VS_2, transport measurements were done in an HPC-33 piston pressure cell. The resistance as a function of temperature is shown in Figure 3.8 at a pressure of 1 GPa. The magnitude of the resistance decreases by a factor of three compared to that at ambient pressure. The band gap from the fit between 150-300 K is 40 meV. As the pressure is increased, there is a further decrease in the band gap, to 35 meV at 2.1 GPa, as shown in Figure 3.9.

Transport measurements in the diamond anvil cell were performed at 3.7 and 7.22 GPa. The devices were measured in a two-point configuration. The resistance from the interface between the crystal and contact wires is in this case included in the measured resistance.

From this data, it appears the sample is still likely insulating at 7.22 GPa. An Arrhenius fit above 150 K yields a bandgap of 9 meV, consistent with the trend observed in the piston pressure cell. Figure 3.10 shows the data plotted against the calculated curve from the high temperature fit. The two agree well down to 150 K, below which the resistance remains lower than expected from a trivial insulator. At 1.8 K, there is a 3-4 order of magnitude

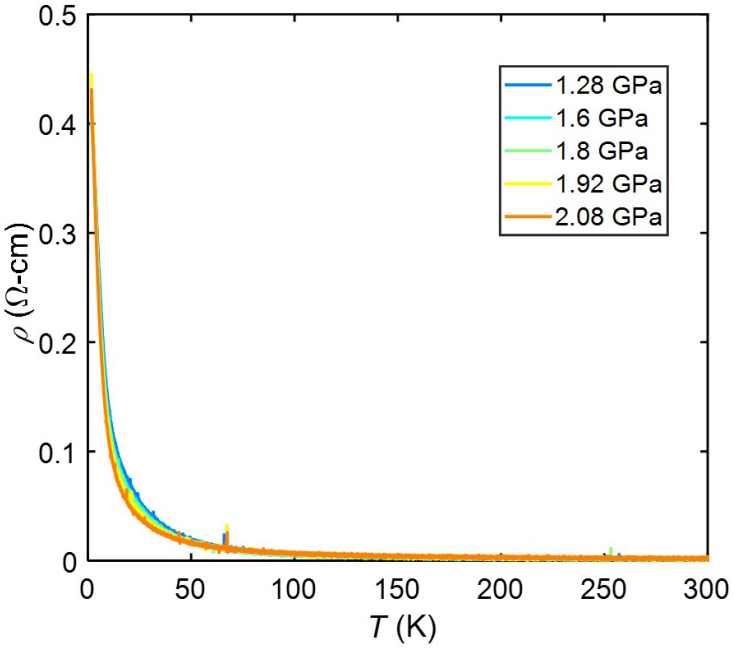

Figure 3.8: Resistivity versus temperature in a HPC-33 piston pressure cell.

difference between the two curves. We note that this appears along with a change in magnetoresistance, with the appearance of a quadratic dependence below 100 K.

We performed powder measurements of magnetization in a SQUID magnetometer down to 1.8 K. The powder sample was mounted on a quartz holder with GE varnish. There is a small magnetic signal, with no signs of a magnetic transition. The increase in low temperatures is attributed to magnetic impurities in the measurement, as the signal is too small to arise from a paramagnetic response from the sample.

The lack of magnetic ordering in Sr-VS_2 suggests there is no antiferromagnetic (AFM) ground state down to 1.8 K. However, localization may still occur in the absence of magnetic order; this is observed in 1T-TaS_2, which forms a 13×13 Star of David pattern which leads to insulating behavior. 1T-TaS_2 is further proposed to be a candidate quantum spin liquid (and further a superconducting phase appears under applied pressure) [57].

3.3 Discussion and Conclusion

We investigated superlattice system Sr-VS_2, grown by solid-state reaction and studied through transport measurements. The crystals are insulating with a small bandgap, which decreases as pressure is applied. At low temperatures, there is evidence for mobile carriers. We observe

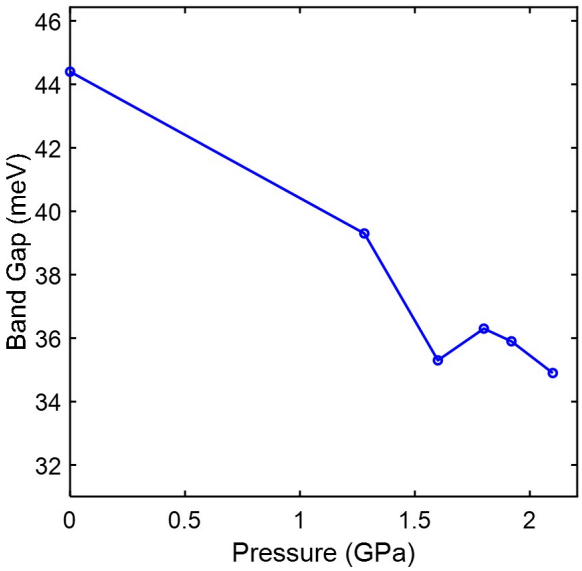

Figure 3.9: Bandgap as a function of pressure in the piston cell.

a deviation from Arrhenius hopping in resistivity and an onset of quadratic MR. Further probes of the material are needed to determine the mechanism. Raman spectroscopy and X-ray diffraction can provide insight into potential structural distortions that may occur. Further measurements under pressure and with chemical doping are of significant interest. A key goal in these systems is to evaluate if such tuning may enable superconductivity therein.

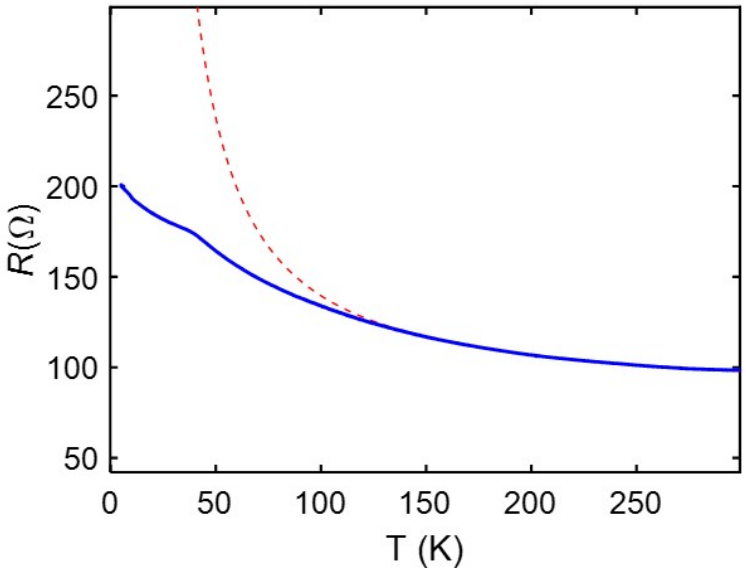

Figure 3.10: Resistance in the DAC, shown in blue. Fit to the band gap at high temperatures shown in red.

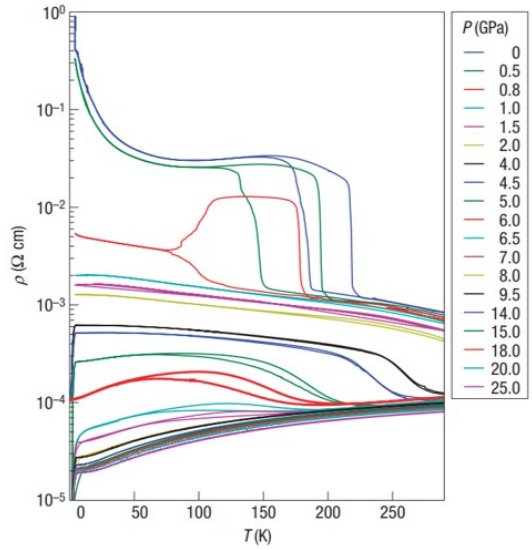

Figure 3.11: Resistivity of $1T$-TaS_2 as a function of pressure. Adapted from [57].

Chapter 4

Group VI TMD superlattices

4.1 Growth attempts

We have attempted syntheses of Group VI semiconducting TMD superlattices through solid-state growth and chemical vapor transport (CVT). The results of the growth attempts and some of the differences between them and the Group V superlattice growths are discussed.

4.1.1 MoS_2

Growths of Ba-MoS_2 produce a product primarily consisting of a mix of dark powder mixed with lustrous crystals with hexagonal facets. PXRD on the product reveals peaks matching that of MoS_2 with some weaker peaks matching that of BaS. This suggests that the growth produced MoS_2. The CVT growth also produced small crystals within a lustrous powder that did not show signs of superlattice peaks in PXRD. The crystals separated from the growths are on the order of 10 microns in size. In the CVT tube, much of the starting material was not transported to the cold end of the tube, indicating an insufficient amount of transport agent. A growth of Sr-MoS_2 yielded similar results, with MoS_2 and SrS in the product.

There are no signs of significant mixing between the Ba and parent TMD. Many alkali metals have been intercalated into Group VI TMDs, such as $NaMoS_2$ and $LiMoS_2$ [58]. In these intercalations, there is some charge transfer between the positive alkali ions and parent compound. In addition, the intercalated atoms have small radii, which allow them to diffuse into gaps between the TMD layers. This generally occurs in a disordered fashion. Alkaline earth metals are less frequently intercalated, which suggests chemical substitution of Group V with Group VI elements in the superlattices may be chemically unfavorable.

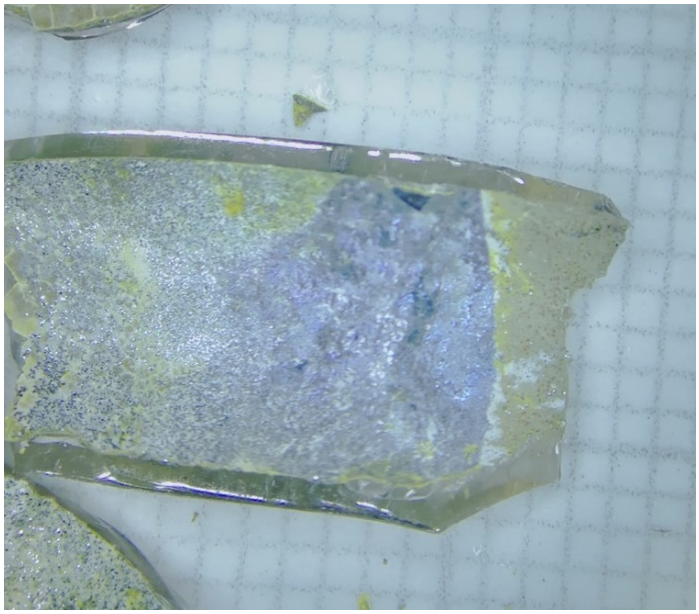

Figure 4.1: Growth attempt of Ba-MoS_2. Powders are seen on the quartz tube wall. Small hexagonal crystals are embedded within the product.

4.1.2 WS_2

The growth of Sr-WS_2 and Ba-WS_2 yielded similar products. XRD reveals the presence of WS_2 and SrS, which indicates the lack of reaction between the precursor material. This chemical trend is also reflected in misfit compounds, where the intercalation of rock salts into Group V TMDs is common, while Group VI TMDs are rare. In misfit compounds, there is charge transfer between the layers that leads to a stable structure. The unfilled bands in Group V TMDs may be more readily doped.

4.1.3 TiS_2

The synthesis of a Ba-TiS_2 superlattice was attempted in similar fashion to those above. The growth of Ba-TiS_2 resulted in a mixed powder with stained inner quartz tube. The stained quartz was dark yellow to orange in color, and it suggests a reaction between the precursors and the quartz. Future attempts of this growth will require a crucible to limit the devitrification.

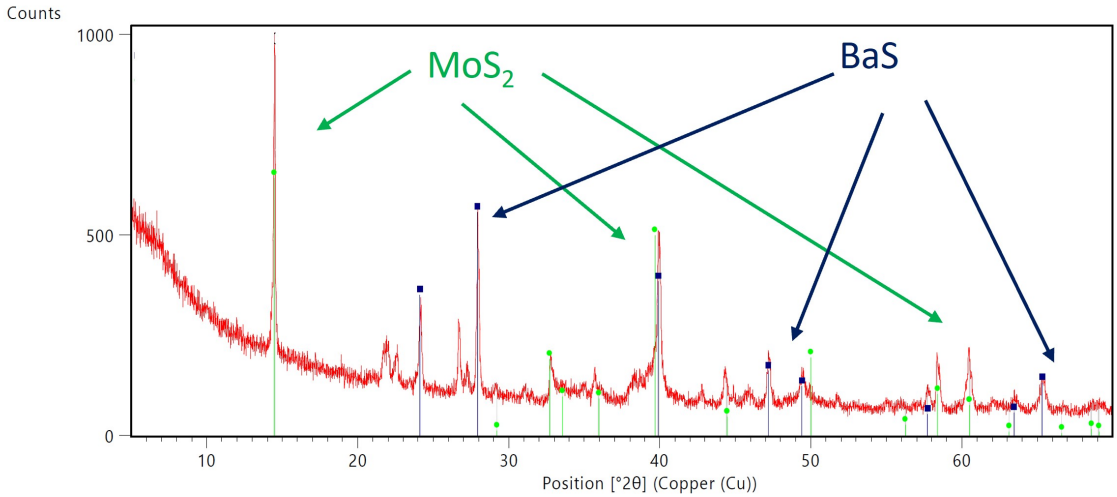

Figure 4.2: XRD of MoS_2. The diffraction peaks are matched to that of MoS_2 and BaS.

4.1.4 CrS_2

The synthesis of a Sr-CrS_2 and Ba-CrS_2 superlattice was attempted in similar fashion to those above. The growth of Sr-CrS_2 resulted in a mixed powder with a dark inner quartz tube. The interior product contained whisker-like threads that may have come from a reaction between the tube and the precursor materials. Future attempts of this growth will require a crucible to limit the devitrification.

4.2 Discussion and Conclusions

Further work lies ahead in the synthesis of Group-VI superlattices. One challenge affecting the synthesis is the additional d electron in the Group VI TMDs, which changes the chemistry involved in the synthesis reactions. It may also be that the filled bands of the semiconducting TMDs are unsuited to accepting or donating charges between the spacer layer, decreasing the stability. Further exploration in the quartenary phase diagram may be needed to find the region favorable for nucleation. Both Mo and W have high melting points, with W the highest among Group V and VI metals. It is notable that in the literature, there is a paucity of reports to our knowledge on Group VI TMD misfit compounds [59][60]. The TMDs involved may be more thermodynamically stable, in which case alternate synthesis methods will be required. One pathway may be through intercalation, which has been done through electrochemistry or vapor transport. There are existing recipes to stabilize other polytopes of semiconducting TMDs, such as *1T* or *1T'* [61].

Chapter 5

Conclusions

In this thesis, we have investigated several members in a family of natural TMD superlattices that are potentially host to a variety of electronic properties. The synthesis of several of these compounds suggests other superlattices are possible and waiting to be explored. We shed light on some of the next steps for Sr-VS_2, and we discuss some of the chemical motifs that may guide further synthesis steps.

5.1 Summary of 2D superlattices

Sr-VS_2 has been successfully synthesized and characterized with transport, magnetization, and pressure. The crystals exhibit insulating behavior with a small bandgap and is possibly due to a Mott insulator phase. From previous calculations, it appears unlikely that the compound is a trivial band insulator. This leaves it open to tuning through other parameters.

Figure 5.1 shows a summary of the various growths attempted in this thesis and in literature, organized by the host TMD layer. An immediate observation in this table is the contrast between Group V and Group VI TMDs. We have successfully synthesized several compounds, all containing the Group V TMDs (MS_2, M = V, Nb, Ta). As discussed in Chapter 4, this trend is reflected in literature on other compounds, such as the misfits. A further investigation into the chemistry and reaction pathways may give insight into this sharp contrast between two related material families.

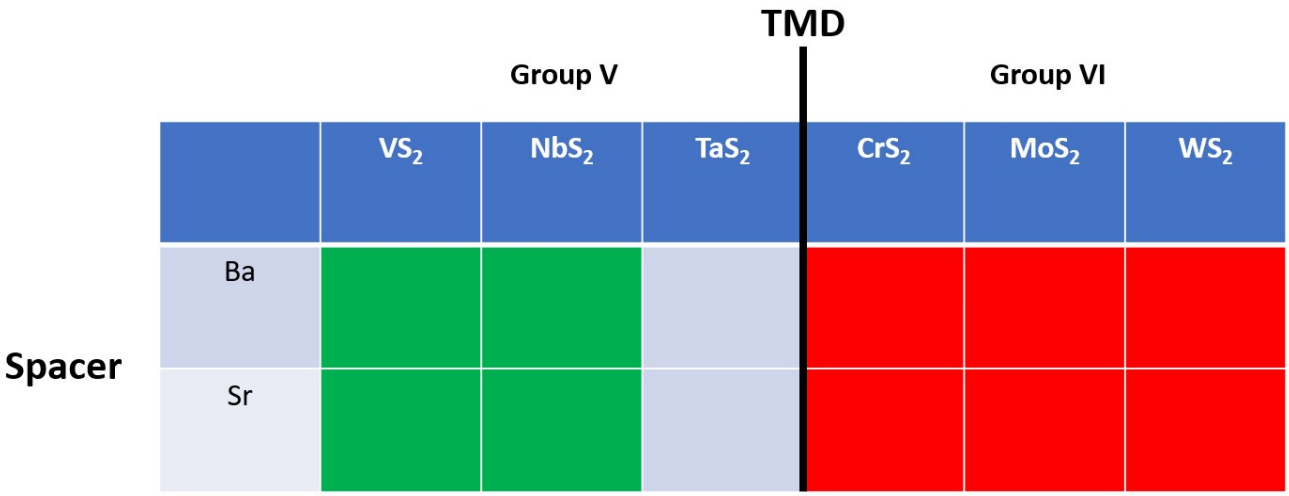

Figure 5.1: Summary of different TMD superlattices growths.

5.2 Perspectives

One takeaway of the results in this work is the ability for to engineer the constituents in a layered bulk crystal. One can in principle design TMD "heterostructures" in an analagous fashion to the 2D vdW heterostructures created using a tear-and-stack method in the monolayer limit. A natural question is whether it is possible to control the number of layers or the stacking order of the TMD. This would give implicit control over symmetries in the system, which can change allowed superconducting order parameters or optical selection rules. The chemical composition can also be utilized to generate interface effects, such as with magnetic atoms as attempted in this thesis, or with topological materials such as Bi_2Se_3. TMDs have various polytypes, and it would be desirable to control or combine such polytypes at will. Many are metastable in their bulk form; it remains to be seen whether their stability can be realized in this superlattice geometry. Finally, the possibility of creating such lattices with long-range modulations, akin to a moire lattice, is also of significant interest. The ability to probe such behavior in a bulk material would open new experimental probes to further our understanding of those states.

An equally exciting property of these superlattice compounds is the ability to exfoliate them. This enables many techniques available to 2D materials, such as electrostatic gating. The spacer layers in materials such as $Ba_6Nb_{11}S_{28}$ may serve as encapsulation in a similar manner as hBN. As such, the layered compounds can be viewed as positioned at the intersection of two worlds, giving them access to both 3D and 2D characterization and manipulation.

An exciting prospect for this work is exfoliation of Sr-VS_2 to enable its further manipulation.

References

[1] G. Grüner, "The dynamics of charge-density waves," *Reviews of modern physics*, vol. 60, no. 4, p. 1129, 1988.

[2] M. J. Manfra, "Molecular beam epitaxy of ultra-high-quality AlGaAs/GaAs heterostructures: Enabling physics in low-dimensional electronic systems," *Annu. Rev. Condens. Matter Phys.*, vol. 5, no. 1, pp. 347–373, 2014.

[3] B. Miksch, A. Pustogow, M. J. Rahim, A. A. Bardin, K. Kanoda, J. A. Schlueter, R. Hübner, M. Scheffler, and M. Dressel, "Gapped magnetic ground state in quantum spin liquid candidate κ-(BEDT-TTF)2Cu2 (CN)3," *Science*, vol. 372, no. 6539, pp. 276–279, 2021.

[4] Y. Liu, N. O. Weiss, X. Duan, H.-C. Cheng, Y. Huang, and X. Duan, "Van der Waals heterostructures and devices," *Nature Reviews Materials*, vol. 1, no. 9, pp. 1–17, 2016.

[5] Y. Yu, L. Ma, P. Cai, R. Zhong, C. Ye, J. Shen, G. D. Gu, X. H. Chen, and Y. Zhang, "High-temperature superconductivity in monolayer $Bi_2Sr_2CaCu_2O_{8+\delta}$," *Nature*, vol. 575, no. 7781, pp. 156–163, 2019.

[6] P. Monceau, "Electronic crystals: an experimental overview," *Advances in Physics*, vol. 61, no. 4, pp. 325–581, 2012.

[7] D. Jérome, "Organic conductors: From charge density wave TTF- TCNQ to superconducting (TMTSF) 2PF6," *Chemical reviews*, vol. 104, no. 11, pp. 5565–5592, 2004.

[8] D. C. Tsui, H. L. Stormer, and A. C. Gossard, "Two-dimensional magnetotransport in the extreme quantum limit," *Physical Review Letters*, vol. 48, no. 22, p. 1559, 1982.

[9] Y. J. Chung, K. Villegas Rosales, K. Baldwin, P. Madathil, K. West, M. Shayegan, and L. Pfeiffer, "Ultra-high-quality two-dimensional electron systems," *Nature Materials*, vol. 20, no. 5, pp. 632–637, 2021.

[10] K. S. Novoselov, A. K. Geim, S. V. Morozov, D. Jiang, M. I. Katsnelson, I. V. Grigorieva, S. Dubonos, Firsov, and AA, "Two-dimensional gas of massless Dirac fermions in graphene," *nature*, vol. 438, no. 7065, pp. 197–200, 2005.

[11] Y. Zhang, Y.-W. Tan, H. L. Stormer, and P. Kim, "Experimental observation of the quantum Hall effect and Berry's phase in graphene," *nature*, vol. 438, no. 7065, pp. 201–204, 2005.

[12] A. Zibrov, E. Spanton, H. Zhou, C. Kometter, T. Taniguchi, K. Watanabe, and A. Young, "Even-denominator fractional quantum Hall states at an isospin transition in monolayer graphene," *Nature Physics*, vol. 14, no. 9, pp. 930–935, 2018.

[13] L. Li, F. Yang, G. J. Ye, Z. Zhang, Z. Zhu, W. Lou, X. Zhou, L. Li, K. Watanabe, T. Taniguchi, *et al.*, "Quantum Hall effect in black phosphorus two-dimensional electron system," *Nature nanotechnology*, vol. 11, no. 7, pp. 593–597, 2016.

[14] F. Sheng, C. Hua, M. Cheng, J. Hu, X. Sun, Q. Tao, H. Lu, Y. Lu, M. Zhong, K. Watanabe, *et al.*, "Rashba valleys and quantum Hall states in few-layer black arsenic," *Nature*, vol. 593, no. 7857, pp. 56–60, 2021.

[15] "Photonics and optoelectronics of 2D semiconductor transition metal dichalcogenides, author=Mak, Kin Fai and Shan, Jie," *Nature Photonics*, vol. 10, no. 4, pp. 216–226, 2016.

[16] S. Tang, C. Zhang, D. Wong, Z. Pedramrazi, H.-Z. Tsai, C. Jia, B. Moritz, M. Claassen, H. Ryu, S. Kahn, *et al.*, "Quantum spin Hall state in monolayer 1T'-WTe_2," *Nature Physics*, vol. 13, no. 7, pp. 683–687, 2017.

[17] X. Xi, Z. Wang, W. Zhao, J.-H. Park, K. T. Law, H. Berger, L. Forró, J. Shan, and K. F. Mak, "Ising pairing in superconducting $NbSe_2$ atomic layers," *Nature Physics*, vol. 12, no. 2, pp. 139–143, 2016.

[18] Y. Cao, V. Fatemi, A. Demir, S. Fang, S. L. Tomarken, J. Y. Luo, J. D. Sanchez-Yamagishi, K. Watanabe, T. Taniguchi, E. Kaxiras, *et al.*, "Correlated insulator behaviour at half-filling in magic-angle graphene superlattices," *Nature*, vol. 556, no. 7699, pp. 80–84, 2018.

[19] C. Jin, E. C. Regan, D. Wang, M. Iqbal Bakti Utama, C.-S. Yang, J. Cain, Y. Qin, Y. Shen, Z. Zheng, K. Watanabe, *et al.*, "Identification of spin, valley and moiré quasi-angular momentum of interlayer excitons," *Nature Physics*, vol. 15, no. 11, pp. 1140–1144, 2019.

[20] Y. Cao, V. Fatemi, S. Fang, K. Watanabe, T. Taniguchi, E. Kaxiras, and P. Jarillo-Herrero, "Unconventional superconductivity in magic-angle graphene superlattices," *Nature*, vol. 556, no. 7699, pp. 43–50, 2018.

[21] E. Y. Andrei, D. K. Efetov, P. Jarillo-Herrero, A. H. MacDonald, K. F. Mak, T. Senthil, E. Tutuc, A. Yazdani, and A. F. Young, "The marvels of moiré materials," *Nature Reviews Materials*, vol. 6, no. 3, pp. 201–206, 2021.

[22] J. Cai, E. Anderson, C. Wang, X. Zhang, X. Liu, W. Holtzmann, Y. Zhang, F. Fan, T. Taniguchi, K. Watanabe, *et al.*, "Signatures of fractional quantum anomalous hall states in twisted $MoTe_2$ bilayer," *arXiv preprint arXiv:2304.08470*, 2023.

[23] C. Park and R. L. Snyder, "Structures of High-Temperature Cuprate Superconductors," *Journal of the American Ceramic Society*, vol. 78, no. 12, pp. 3171–3194, 1995.

[24] A. Devarakonda, H. Inoue, S. Fang, C. Ozsoy-Keskinbora, T. Suzuki, M. Kriener, L. Fu, E. Kaxiras, D. C. Bell, and J. G. Checkelsky, "Clean 2D superconductivity in a bulk van der Waals superlattice," *Science*, vol. 370, no. 6513, pp. 231–236, 2020.

[25] A. Devarakonda, T. Suzuki, S. Fang, J. Zhu, D. Graf, M. Kriener, L. Fu, E. Kaxiras, and J. Checkelsky, "Signatures of bosonic Landau levels in a finite-momentum superconductor," *Nature*, vol. 599, no. 7883, pp. 51–56, 2021.

[26] J. Bardeen, L. N. Cooper, and J. R. Schrieffer, "Theory of superconductivity," *Physical review*, vol. 108, no. 5, p. 1175, 1957.

[27] N. F. Mott, "Conduction in non-crystalline materials: III. Localized states in a pseudogap and near extremities of conduction and valence bands," *Philosophical Magazine*, vol. 19, no. 160, pp. 835–852, 1969.

[28] K. T. Law and P. A. Lee, "1T-TaS_2 as a quantum spin liquid," *Proceedings of the National Academy of Sciences*, vol. 114, no. 27, pp. 6996–7000, 2017.

[29] J. Linder and J. W. Robinson, "Superconducting spintronics," *Nature Physics*, vol. 11, no. 4, pp. 307–315, 2015.

[30] M. Sato and Y. Ando, "Topological superconductors: a review," *Reports on Progress in Physics*, vol. 80, no. 7, p. 076 501, 2017.

[31] C. Beenakker, "Search for Majorana fermions in superconductors," *Annu. Rev. Condens. Matter Phys.*, vol. 4, no. 1, pp. 113–136, 2013.

[32] C. Van Efferen, J. Berges, J. Hall, E. Van Loon, S. Kraus, A. Schobert, T. Wekking, F. Huttmann, E. Plaar, N. Rothenbach, *et al.*, "A full gap above the Fermi level: the charge density wave of monolayer VS_2," *Nature Communications*, vol. 12, no. 1, p. 6837, 2021.

[33] M. Kan, B. Wang, Y. H. Lee, and Q. Sun, "A density functional theory study of the tunable structure, magnetism and metal-insulator phase transition in VS_2 monolayers induced by in-plane biaxial strain," *Nano Research*, vol. 8, pp. 1348–1356, 2015.

[34] D. W. Murphy, C. Cros, F. J. Di Salvo, and J. Waszczak, "Preparation and properties of Li_xVS_2 ($0 \leq x \leq 1$)," *Inorganic Chemistry*, vol. 16, no. 12, pp. 3027–3031, 1977.

[35] R. Yan, G. Khalsa, B. T. Schaefer, A. Jarjour, S. Rouvimov, K. C. Nowack, H. G. Xing, and D. Jena, "Thickness dependence of superconductivity in ultrathin NbS_2," *Applied Physics Express*, vol. 12, no. 2, p. 023 008, 2019.

[36] N. Ghimire, M. A. McGuire, D. S. Parker, B. Sipos, S. Tang, J.-Q. Yan, B. C. Sales, and D. Mandrus, "Magnetic phase transition in single crystals of the chiral helimagnet $Cr_{1/3}NbS_2$," *Physical Review B*, vol. 87, no. 10, p. 104 403, 2013.

[37] S. Wu, Z. Xu, S. C. Haley, S. F. Weber, A. Acharya, E. Maniv, Y. Qiu, A. Aczel, N. S. Settineri, J. B. Neaton, *et al.*, "Highly Tunable Magnetic Phases in Transition-Metal Dichalcogenide $Fe_{1/3+\delta}$ NbS_2," *Physical Review X*, vol. 12, no. 2, p. 021 003, 2022.

[38] S. S. Ataei, D. Varsano, E. Molinari, and M. Rontani, "Evidence of ideal excitonic insulator in bulk MoS_2 under pressure," *Proceedings of the National Academy of Sciences*, vol. 118, no. 13, e2010110118, 2021.

[39] N. Leisgang, S. Shree, I. Paradisanos, L. Sponfeldner, C. Robert, D. Lagarde, A. Balocchi, K. Watanabe, T. Taniguchi, X. Marie, *et al.*, "Giant Stark splitting of an exciton in bilayer MoS_2," *Nature Nanotechnology*, vol. 15, no. 11, pp. 901–907, 2020.

[40] A. Sebastian, R. Pendurthi, T. H. Choudhury, J. M. Redwing, and S. Das, "Benchmarking monolayer MoS_2 and WS_2 field-effect transistors," *Nature communications*, vol. 12, no. 1, p. 693, 2021.

[41] K. Kang, S. Xie, L. Huang, Y. Han, P. Y. Huang, K. F. Mak, C.-J. Kim, D. Muller, and J. Park, "High-mobility three-atom-thick semiconducting films with wafer-scale homogeneity," *Nature*, vol. 520, no. 7549, pp. 656–660, 2015.

[42] D. Unuchek, A. Ciarrocchi, A. Avsar, Z. Sun, K. Watanabe, T. Taniguchi, and A. Kis, "Valley-polarized exciton currents in a van der Waals heterostructure," *Nature nanotechnology*, vol. 14, no. 12, pp. 1104–1109, 2019.

[43] D. Rhodes, S. H. Chae, R. Ribeiro-Palau, and J. Hone, "Disorder in van der Waals heterostructures of 2D materials," *Nature materials*, vol. 18, no. 6, pp. 541–549, 2019.

[44] K. I. Bolotin, F. Ghahari, M. D. Shulman, H. L. Stormer, and P. Kim, "Observation of the fractional quantum Hall effect in graphene," *Nature*, vol. 462, no. 7270, pp. 196–199, 2009.

[45] B. E. Feldman, B. Krauss, J. H. Smet, and A. Yacoby, "Unconventional sequence of fractional quantum hall states in suspended graphene," *Science*, vol. 337, no. 6099, pp. 1196–1199, 2012.

[46] F. Cadiz, E. Courtade, C. Robert, G. Wang, Y. Shen, H. Cai, T. Taniguchi, K. Watanabe, H. Carrere, D. Lagarde, *et al.*, "Excitonic linewidth approaching the homogeneous limit in MoS 2-based van der Waals heterostructures," *Physical Review X*, vol. 7, no. 2, p. 021 026, 2017.

[47] F. Gamble, J. H. Osiecki, M. Cais, R. Pisharody, F. DiSalvo, and T. Geballe, "Intercalation complexes of Lewis bases and layered sulfides: a large class of new superconductors," *Science*, vol. 174, no. 4008, pp. 493–497, 1971.

[48] J. Rouxel, A. Meerschaut, and G. Wiegers, "Chalcogenide misfit layer compounds," *Journal of alloys and compounds*, vol. 229, no. 1, pp. 144–157, 1995.

[49] D. R. Merrill, D. B. Moore, S. R. Bauers, M. Falmbigl, and D. C. Johnson, "Misfit layer compounds and ferecrystals: Model systems for thermoelectric nanocomposites," *Materials*, vol. 8, no. 4, pp. 2000–2029, 2015.

[50] G. R. Reisinger and K. W. Richter, "Review of vanadium-based layered compounds," *Journal of Alloys and Compounds*, vol. 891, p. 161 976, 2022.

[51] *Model sr830 dsp lock-in amplifier*, 2.1, Stanford Research Systems, 1993.

[52] *User guide pressure cell model number hpc-33 revision c*, Quantum Design Japan.

[53] E. Ohmichi and T. Osada, "Torque magnetometry in pulsed magnetic fields with use of a commercial microcantilever," *Review of Scientific Instruments*, vol. 73, no. 8, pp. 3022–3026, 2002.

[54] A. Gauzzi, A. Sellam, G. Rousse, Y. Klein, D. Taverna, P. Giura, M. Calandra, G. Loupias, F. Gozzo, E. Gilioli, *et al.*, "Possible phase separation and weak localization in the absence of a charge-density wave in single-phase 1 T-VS_2," *Physical Review B*, vol. 89, no. 23, p. 235 125, 2014.

[55] L. Cario, B. Corraze, A. Meerschaut, and O. Chauvet, "Dielectric breakdown and current switching effect in the incommensurate layered compound (La S)$_1$.196 VS_2," *Physical Review B*, vol. 73, no. 15, p. 155 116, 2006.

[56] A. Ino, T. Okane, S.-I. Fujimori, A. Fujimori, T. Mizokawa, Y. Yasui, T. Nishikawa, and M. Sato, "Evolution of the electronic structure from electron-doped to hole-doped states in the two-dimensional Mott-Hubbard system $La_{1.17-x}$ Pb_x $VS_{3.17}$," *Physical Review B*, vol. 69, no. 19, p. 195 116, 2004.

[57] B. Sipos, A. F. Kusmartseva, A. Akrap, H. Berger, L. Forró, and E. Tutiš, "From Mott state to superconductivity in 1T-TaS_2," *Nature materials*, vol. 7, no. 12, pp. 960–965, 2008.

[58] F. Xiong, H. Wang, X. Liu, J. Sun, M. Brongersma, E. Pop, and Y. Cui, "Li intercalation in MoS_2: in situ observation of its dynamics and tuning optical and electrical properties," *Nano letters*, vol. 15, no. 10, pp. 6777–6784, 2015.

[59] M. A. Choffel, R. N. Gannon, F. Göhler, A. M. Miller, D. L. Medlin, T. Seyller, and D. C. Johnson, "Synthesis and electrical properties of a new compound $(BiSe)_{0.97}$ $(Bi_2Se_3)_{1.26}$ $(BiSe)_{0.97}$ $(MoSe_2)$ containing metallic 1T-$MoSe_2$," *Chemistry of Materials*, vol. 33, no. 16, pp. 6403–6411, 2021.

[60] M. A. Choffel, T. M. Kam, and D. C. Johnson, "Substituent Effects in the Synthesis of Heterostructures," *Inorganic Chemistry*, vol. 60, no. 13, pp. 9598–9606, 2021.

[61] Y. Yu, G.-H. Nam, Q. He, X.-J. Wu, K. Zhang, Z. Yang, J. Chen, Q. Ma, M. Zhao, Z. Liu, *et al.*, "High phase-purity 1T'-MoS_2-and 1T'-$MoSe_2$-layered crystals," *Nature chemistry*, vol. 10, no. 6, pp. 638–643, 2018.